

**Magnetism of kagome metals ( $\text{Fe}_{1-x}\text{Co}_x$ ) Sn studied by  $\mu\text{SR}$** 

Yipeng Cai<sup>1,2,3,\*</sup>, Sungwon Yoon<sup>3,4</sup>, Qi Sheng,<sup>1</sup> Guoqiang Zhao<sup>1,5</sup>, Eric Francis Seewald<sup>1</sup>,  
Sanat Ghosh<sup>1</sup>, Julian Ingham,<sup>1</sup> Abhay Narayan Pasupathy<sup>1</sup>, Raquel Queiroz<sup>1</sup>, Hechang Lei,<sup>6</sup>  
Yaofeng Xie,<sup>7</sup> Pengcheng Dai<sup>7,8</sup>, Takashi Ito,<sup>9</sup> Ruyi Ke<sup>10</sup>, Robert J. Cava<sup>10</sup>, Sudarshan Sharma<sup>11</sup>,  
Mathew Pula<sup>11</sup>, Graeme M. Luke<sup>3,11</sup>, Kenji M. Kojima,<sup>2,3</sup> and Yasutomo J. Uemura<sup>1,†</sup>

<sup>1</sup>*Department of Physics, Columbia University, New York, New York 10027, USA*

<sup>2</sup>*Quantum Matter Institute, University of British Columbia, Vancouver, British Columbia, Canada V6T 1Z4*

<sup>3</sup>*TRIUMF, Vancouver, British Columbia V6T 2A3, Canada*

<sup>4</sup>*Department of Physics, Sungkyunkwan University, Suwon 16419, Republic of Korea*

<sup>5</sup>*Institute of Physics, Chinese Academy of Sciences, Beijing 100190, China*

<sup>6</sup>*Department of Physics and Beijing Key Laboratory of Opto-Electronic Functional Materials & Micro-Nano Devices, Renmin University of China, Beijing, China*

<sup>7</sup>*Department of Physics and Astronomy, Rice University, Houston, Texas, USA*

<sup>8</sup>*Smalley-Curl Institute, Rice University, Houston, Texas, USA*

<sup>9</sup>*Advanced Science Research Centre, Japan Atomic Energy Agency (JAEA), Tokai, Naka, Ibaraki 319-1195, Japan*

<sup>10</sup>*Department of Chemistry, Princeton University, Princeton, New Jersey 08540, USA*

<sup>11</sup>*Department of Physics and Astronomy, McMaster University, Hamilton, Ontario, Canada L8S 4M1*



(Received 18 October 2024; revised 24 April 2025; accepted 16 May 2025; published 5 June 2025)

We study the magnetic properties of the metallic kagome system  $(\text{Fe}_{1-x}\text{Co}_x)\text{Sn}$  by a combination of muon spin relaxation ( $\mu\text{SR}$ ), magnetic susceptibility, and scanning tunneling microscopy (STM) measurements in single crystal specimens with Co concentrations  $x = 0, 0.11, 0.8$ . In the undoped antiferromagnetic compound FeSn, we find possible signatures for a previously unidentified phase that sets in at  $T^* \sim 50$  K, well beneath the Neel temperature  $T_N \sim 376$  K, as indicated by a peak in the relaxation rate  $1/T_1$  observed in zero field (ZF) and longitudinal field (LF)  $\mu\text{SR}$  measurements, with a corresponding anomaly in the ac and dc susceptibility, and an increase in the static width  $1/T_2$  in ZF- $\mu\text{SR}$  measurements. No signatures of spatial symmetry breaking are found in STM down to 7 K. Related to the location and motion of muons in FeSn, we confirm a previous report that about 40% of the implanted muons reside at a field-cancelling high symmetry site at  $T < 250$  K, while an onset of thermal hopping changes the site occupancy at higher temperatures. In  $\text{Fe}_{0.89}\text{Co}_{0.11}\text{Sn}$ , where disorder eliminates the field-cancellation effect, all the implanted muons exhibit precession and/or relaxation in the ordered state. In  $\text{Fe}_{0.2}\text{Co}_{0.8}\text{Sn}$ , we find canonical spin glass behavior with freezing temperature  $T_g \sim 3.5$  K; the ZF- and LF- $\mu\text{SR}$  time spectra exhibit results similar to those observed in dilute alloy spin glasses CuMn and AuFe, with a critical behavior of  $1/T_1$  at  $T_g$  and  $1/T_1 \rightarrow 0$  as  $T \rightarrow 0$ . The absence of spin dynamics at low temperatures makes a clear contrast to the spin dynamics observed by  $\mu\text{SR}$  in many geometrically frustrated spin systems on insulating kagome, pyrochlore, and triangular lattices. The spin glass behavior of CoSn doped with dilute Fe moments is shown to originate primarily from the randomness of doped Fe moments rather than due to geometrical frustration of the underlying lattice.

DOI: [10.1103/PhysRevB.111.214412](https://doi.org/10.1103/PhysRevB.111.214412)

**I. INTRODUCTION**

Geometrically frustrated magnets are excellent candidate materials for exploring exotic physics, since conventional magnetic orders are suppressed. Antiferromagnetically interacting spins in such systems—including the triangular, kagome, and pyrochlore lattices—produce highly degenerate ground states without magnetic long-range order, resulting in tendencies toward quantum spin liquids or spin glass freezing [1–8]. For this reason, Mott insulating kagome materials such as herbertsmithite, volborthite, and barlowite have been studied as candidate spin liquids [9–11].

Yet, in recent years, metallic kagome systems have become a major subfield of condensed matter physics. Their band structure naturally hosts Dirac points, flat bands, and van Hove singularities with an unusual sublattice structure, making kagome metals a natural setting for strong correlations and band topology to interplay [12,13]; indeed, many studies have proposed these systems to host various unconventional correlated phases [14–25]. For this reason, in the last ten years experiments have explored materials comprised of stacks of metallic kagome layers in search of evidence for interesting electronic phase transitions, the recent history of which begins with the discovery of half Heusler compounds  $\text{Mn}_3\text{Sn}$  and  $\text{Mn}_3\text{Ge}$ —antiferromagnets exhibiting a magneto-optical Kerr effect and large anomalous Hall effect despite zero net magnetization [26–29]—and of  $\text{Co}_3\text{Sn}_2\text{S}_2$  soon thereafter—a Weyl

\*Contact author: caidia52@gmail.com

†Contact author: yu2@columbia.edu

semimetal hosting a large anomalous Hall effect and surface nematic order [30–33]. Yet these materials are relatively three-dimensional, making the role of the two-dimensional kagome motif in their interesting properties somewhat unclear.

In 2018, intermetallic compound  $\text{Fe}_3\text{Sn}_2$  was discovered with a similar structure to  $\text{Co}_3\text{Sn}_2\text{S}_2$  [34,35]. Compared to the 3:1 intermetallics, these materials are more two-dimensional, and exhibit some aspects of the two-dimensional kagome physics. Experiments have shown evidence of massive Dirac fermions gapped out by ferromagnetism with an associated large intrinsic Hall conductivity [34,36]. The Dirac pockets can be manipulated by magnetic fields [35], along with skyrmion bubbles [37–39] and a nematic response to external magnetic fields [40]. Building on this work, the 1:1 intermetallics  $\text{FeSn}$  [41] and  $\text{CoSn}$  [42] were found to exhibit significantly less three-dimensionality compared to the 3:1 and 3:2 structures. ARPES reports the appearance of a relatively flat band whose dispersion is suppressed along both the in- and out-of-plane directions, exhibiting a bandwidth of  $\sim 150$  meV roughly 300 meV beneath the Fermi level in  $\text{CoSn}$  [42], although inelastic neutron scattering experiments were unable to identify the expected flat spin excitations from electron-hole excitations of electronic flat bands [43]. The relatively flat band exists above the Fermi level in the case of  $\text{FeSn}$ ; interpolating between the two compounds with  $\text{Fe}_x\text{Co}_{1-x}\text{Sn}$  for  $0 < x < 1$  produces an interesting phase diagram hosting spin glass behavior and nontrivial antiferromagnetic order [44,45]. Tunneling experiments on  $\text{FeSn}$  have seen evidence of a relatively flat band existing in the surface band structure, even though the kagome flat band is further away in the bulk [46], coexisting with Weyl fermionic surface states [47], and recent work has seen interesting nematic charge patterns in scanning tunneling microscopy (STM) [48].

In parallel, an immense amount of recent attention has also been devoted to the 166 family  $\text{RM}_6\text{X}_6$ , including the frustrated charge density wave materials  $\text{ScV}_6\text{Sn}_6$  and  $\text{LuNb}_6\text{Sn}_6$  [49–57], as well as the unconventional superconductors of the 135 family  $\text{AV}_3\text{Sb}_5$  ( $A = \text{K}, \text{Rb}, \text{Cs}$ ), which exhibit nematic order alongside signatures of time-reversal symmetry breaking and multiple distinct density wave orders [58–73]. A unifying theme in all these systems is the need to understand the nature of electronic symmetry breaking in the kagome lattice geometry and its relation to unconventional superconductivity or magnetism.

To further understand how electronic and magnetic orders evolve in kagome metals and the underlying mechanisms behind correlated phases, we investigate the kagome metal  $\text{FeSn}$ , shown in Fig. 1, and explore how its magnetic properties are turned by Co substitution.  $\text{FeSn}$  features a layered kagome structure in which Fe moments align ferromagnetically within each plane and alternate between planes, forming an A-type antiferromagnetic order below the Neel temperature  $T_N \sim 376$  K. Although  $\text{FeSn}$  shares the same crystal structure and high temperature magnetic ordering as  $\text{FeGe}$ , it notably lacks the charge density wave (CDW) formation as observed in the latter [74], raising questions about the role of electron/magnetic correlations in these materials. To probe this further, we study the solid solution series  $(\text{Fe}_{1-x}\text{Co}_x)\text{Sn}$ , which forms a continuous kagome lattice with tunable magnetic behavior. Work by Sales

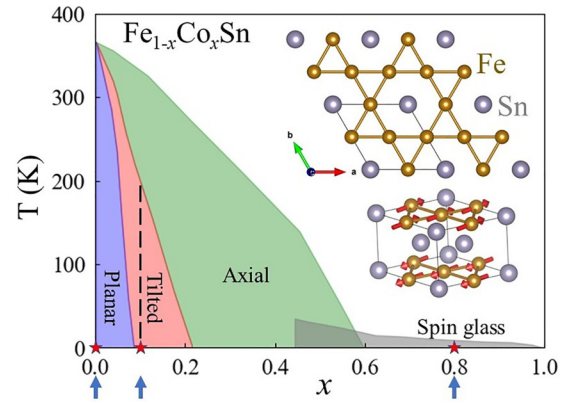


FIG. 1. Magnetic phase diagram of  $(\text{Fe}, \text{Co})\text{Sn}$  [45]. Red stars with blue arrow marks on the horizontal axis show the corresponding Co concentrations in our studies. Inset shows the kagome layer in the  $\text{FeSn}$  crystal structure and its magnetic structure below  $T_N$ .

*et al.* [45] mapped out a rich phase diagram, Fig. 1, showing a rapid suppression of magnetic order with increasing Co concentration and a reorientation of the ordered moments from in plane to out of plane. Near the percolation threshold at  $x \sim 0.5$ , the system transitions to a spin-glass-like regime, with freezing temperatures  $T_g$  scale linearly with Fe concentration  $x$ . These observations motivate our study of how Co doping modulates the competing interactions in  $\text{FeSn}$ , with the aim of understanding the emergence of spin glass behavior in kagome metals.

To study details of magnetic properties, muon spin relaxation ( $\mu\text{SR}$ ) [75] is a powerful and unique probe which can detect (a) the volume fraction of magnetically ordered regions in a phase-separated system, (b) static spin freezing of uniform or random spin configurations even with a very small ordered moment size, and (c) dynamic spin fluctuations in a wide fluctuation time window. A pioneering  $\mu\text{SR}$  study by Hartmann and Wappling in the 1980s reported that in  $\text{FeSn}$ , approximately 60% of implanted muons experienced a local field strength of  $\sim 0.21$  T, while the remaining 40% appears to reside at a field cancellation site below 250 K [76]. We reexamined and performed detailed  $\mu\text{SR}$  measurements to further address the magnetic properties of  $\text{FeSn}$  and its evolution with Co doping. In this paper, we report studies of  $\text{Fe}_{1-x}\text{Co}_x\text{Sn}$  with three concentrations  $x = 0, 0.11$ , and  $0.8$ , which exhibit, respectively, a planar magnetic ordered state, a complex reorientation ordered moment state, and a spin glass state at low temperature [45,77].

The present paper contributes to two different research fronts: (1) providing information on the materials properties of  $(\text{Fe}, \text{Co})\text{Sn}$  by  $\mu\text{SR}$ , magnetic susceptibility, and STM; and (2) adding information on the location and motion of muons in the material and to advance the methodology of the  $\mu\text{SR}$  technique. In Secs. III A 2 and III A 4, we report a discovery of an anomaly at  $T \sim 50$  K in  $1/T_1$  and  $1/T_2$  measurements of  $\mu\text{SR}$  (in Fig. 7) in undoped  $\text{FeSn}$ , corresponding data from magnetic susceptibility (in Fig. 8), and STM studies (in Figs. 9 and 10). These results could be considered possible signatures of a previously unidentified phase deep in the magnetically ordered state. Section III F shows the  $\mu\text{SR}$  results

in a Co-rich sample of  $x = 0.8$ , which exhibits a spin glass behavior. The zero field (ZF) and longitudinal field (LF)  $\mu$ SR measurements show spin freezing associated with the slowing down of spin fluctuations toward the freezing temperature  $T_g \sim 3.5$  K, while dynamic spin fluctuations die away at low temperatures well below  $T_g$ . Comparisons of these results with  $\mu$ SR and susceptibility data from a kagome lattice spin system  $\text{SrCr}_8\text{Ga}_4\text{O}_{19}$  (SCGO), described in Sec. IV B, demonstrate that (Fe,Co)Sn in the spin glass region exhibits behavior similar to those of the canonical dilute alloy spin glasses AuFe and CuMn, without persistent spin dynamics [78] often observed in insulating magnetic systems on geometrically frustrated kagome, triangular, and/or pyrochlore lattices.

Regarding the second research front with muon-specific phenomena, Sec. III A includes detailed  $\mu$ SR data in FeSn obtained in spin-rotated (SR) and non-spin-rotated (NSR) configurations and the field dependence, while Sec. III D introduces simulations for muon site and local magnetic field in FeSn, and the comparisons with the observed data. The  $\mu$ SR results in 11% Co doped  $\text{Fe}_{0.89}\text{Co}_{0.11}\text{Sn}$ , described in Sec. III E, provide an example where the field-cancelling effect is absent due to disorder. General readers interested solely in materials may skip these muon-specific sections, while the detailed data and analyses in these sections provide reliability to the whole results and discussions of the present paper.

## II. EXPERIMENTAL AND NUMERICAL DETAILS

Using methods similar to those described in Ref. [43], high-quality single crystals with  $x = 0$  and 0.11, having a typical size of  $2 \times 2 \times 5$  mm<sup>3</sup>, were prepared at Renmin University of China, while  $x = 0.8$  was prepared at Rice University. We collected magnetic susceptibility measurements from 1.9 K to 300 K on a small single crystal using a Quantum Design Magnetic Property Measurement System XL-3. We also measured the resistivity on a single crystal between 1.9 K and 300 K using a Quantum Design Physical Property Measurement System. The STM measurements were performed on FeSn crystals used in  $\mu$ SR studies, cleaved under ultrahigh vacuum inside the STM chamber and scanned at low temperatures  $\sim 7$  K.

The  $\mu$ SR experiments were performed at TRIUMF in Vancouver, Canada, using a gas flow cryostat on the M20 beamlines for measurements above 2 K on all samples and an Oxford dilution refrigerator on the M15 beamline for measurements below 2 K on  $\text{Fe}_{0.2}\text{Co}_{0.8}\text{Sn}$ . Figure 2 shows the counterconfiguration used in our experiments at the M20 beamline. Mosaic crystals of  $\sim 300$  mg in mass for each concentration were aligned and mounted with their  $c$  axis perpendicular to the beam direction. The  $a$  and  $b$  axes within the  $ab$  plane were not aligned and remained randomly oriented. We used two different measurement modes: NSR and SR, as illustrated in Fig. 2. In the SR mode, the initial muon spin direction was arranged perpendicular to the beam direction, such that the incident muon spins were parallel to the sample  $c$  axis.  $\mu$ SR experiments were performed in ZF, LFs parallel to the initial muon spin polarization, and transverse fields (TFs) perpendicular to that. All  $\mu$ SR data were analyzed in the time domain using the open-source MUSRIT software package [79]. We also employed project augmented

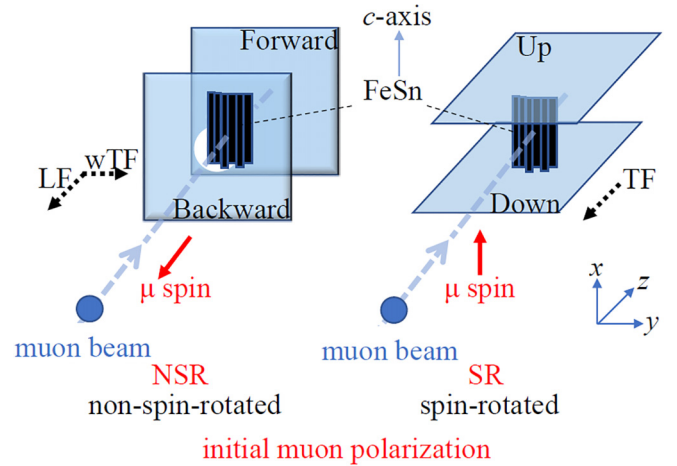


FIG. 2. Geometry of the  $\mu$ SR experiment setup at M20 beamline. Left: Non-spin-rotated mode, where the incident muon spin direction is parallel to the muon beam axis. Right: Spin-rotated mode, where muon spin was rotated and perpendicular to the muon beam axis. External field can be applied accordingly either parallel to the muon spin (LF) or perpendicular to the muon spin (TF). The corresponding pair of counters for collecting positrons are forward/backward (FB) for the NSR and up/down (UD) for the SR mode.

wave (PAW) pseudopotentials with generalized gradient approximation–Perdew–Burke–Ernzerhof (GGA–PBE) from the standard density functional theory (DFT) as implemented in QUANTUM ESPRESSO, where the muon was modeled as a proton to simulate the muon stopping sites.

## III. RESULTS

### A. $\mu$ SR in FeSn

#### 1. Notable features in the time spectra of ZF and TF: Field-cancelling site

In the parent compound FeSn, we started with ZF measurements in both the SR and NSR modes. As shown in both the time and FFT spectra of Fig. 3, the oscillation amplitude observed in the NSR mode is much smaller than that in the SR mode in the antiferromagnetically ordered state. This feature indicates that the local field at the muon stopping site points nearly perpendicular to the  $c$  axis within the  $ab$  plane. If the local field is fully perpendicular to the  $c$  axis, we expect the oscillation amplitude in ZF–NSR to be half that in ZF–SR. As shown later, this field orientation is also consistent with

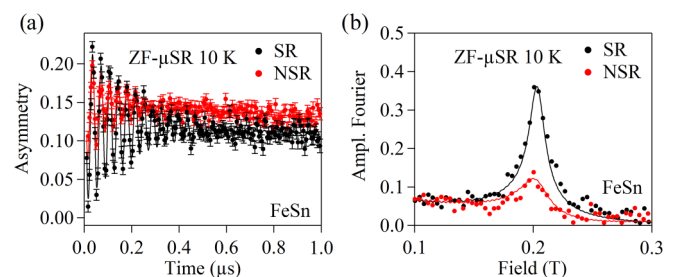


FIG. 3. ZF- $\mu$ SR time spectra in FeSn (a) and corresponding FFT spectra (b) observed in the SR and NSR modes at  $T = 10$  K.

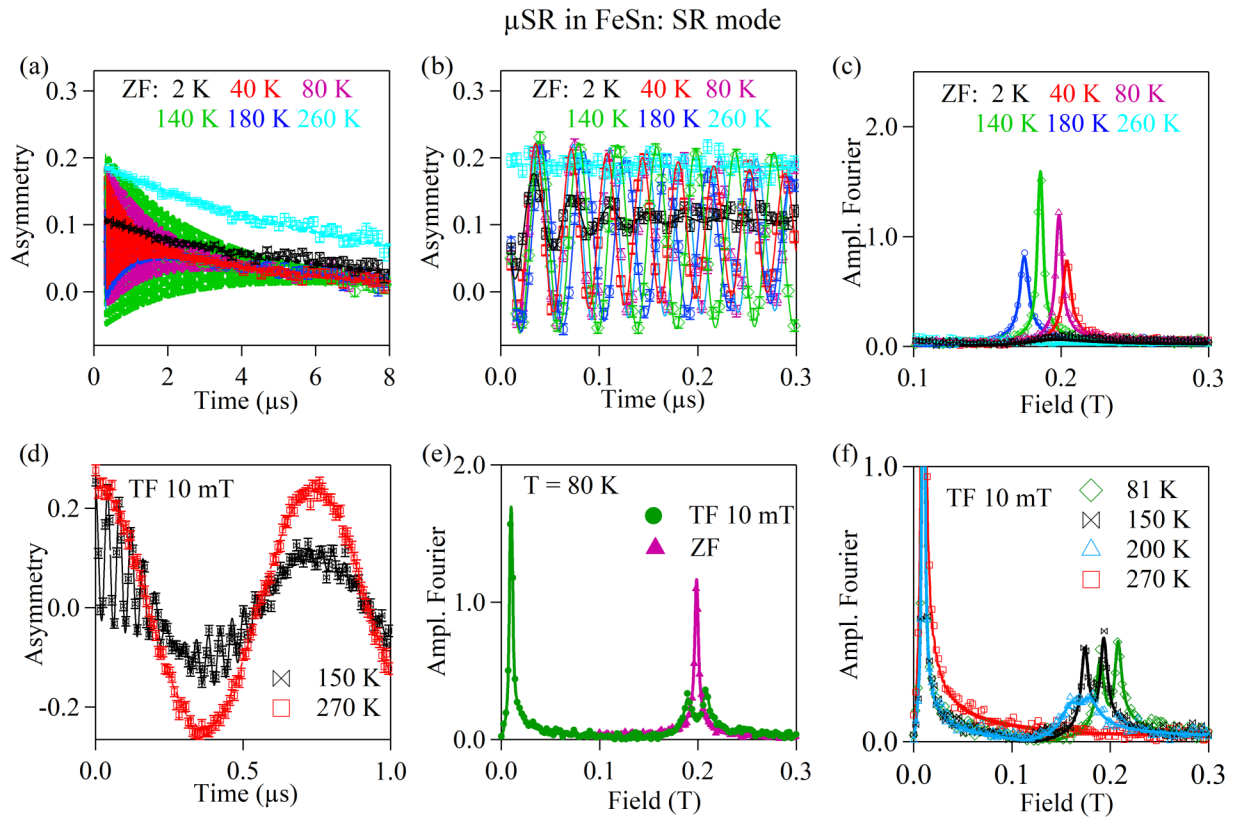


FIG. 4. All lines are fitting results as described in the main text. (a) ZF-SR time spectra of FeSn up to  $8 \mu\text{s}$  at selected temperatures. (b) ZF-SR time spectra of FeSn within  $0.3 \mu\text{s}$ . (c) FFT spectra of FeSn in ZF-SR. (d) wTF-SR time spectra of FeSn with an external TF of  $10 \text{ mT}$ . (e) Comparison of FFT spectra of FeSn in ZF and wTF  $10 \text{ mT}$  at  $80 \text{ K}$ . (f) FFT spectra of FeSn in wTF at selected temperatures.

the planar magnetic structure for the muon site estimated by our calculation. Figures 4(a) and 4(b) show examples of the time spectra observed in the ZF-SR mode at several selected temperature points, in a longer time range up to  $t = 8 \mu\text{s}$  in (a) and a shorter time range of  $0.3 \mu\text{s}$  in (b). Fourier transforms (FFT) of the ZF-SR data shown in Fig. 4(c) indicate that there is only one frequency in the ordered state, corresponding to a local field strength of  $\sim 0.2 \text{ T}$  at the muon stopping site. The precession frequency develops around  $250 \text{ K}$ , well below  $T_N \sim 376 \text{ K}$ , which is likely due to muon diffusion. A significant broadening of the FFT signal is seen below  $50 \text{ K}$ , corresponding to the fast depolarization of the precession signal in Fig. 4(b) at low temperatures.

To check the magnetic volume fraction and any possible phase separations, we then turned to the TF configuration and applied a small transverse field  $10 \text{ mT}$  perpendicular to the  $c$  axis and parallel to the  $ab$  plane. Figure 4(d) shows examples of the time spectra observed in the TF-SR mode. Figure 4(e) compares the FFT spectra observed in ZF and the weak transverse field (wTF) of  $10 \text{ mT}$  at  $T = 80 \text{ K}$ , and Fig. 4(f) shows the FFT spectra obtained at several different temperatures in the wTF configuration. In the FFTs of the wTF data, two high-frequency peaks were observed at an equal distance from the ZF frequency peak, in addition to the low-frequency peak at the applied field of  $10 \text{ mT}$ . The existence of the muon precession component at the applied field frequency in wTF readily indicates that there is a muon population that resides at a site where the static internal field from the ordered moment

cancels or in phase-separated regions which remain paramagnetic. We note that our powder x-ray diffraction measurements at  $300 \text{ K}$  on these crystals reveal no detectable impurity phases or indications of phase separation within the resolution of our experiments. Meanwhile, in the case of  $\text{Fe}_{0.89}\text{Co}_{0.11}\text{Sn}$ , as shown in the subsequent section of the present paper, this field absent site disappears, presumably due to the disorder of the Fe spin network introduced by Co substitutions. This observation strongly suggests that the field absent site in FeSn originates from a cancellation of static local fields from the ordered Fe moments at certain muon sites.

## 2. Analyses of ZF/wTF $\mu\text{SR}$ : Anomalies at low temperatures

We fit the ZF time spectra with a function assuming one oscillation frequency  $\gamma_\mu B_{\text{int}}$ ,

$$A(t) = A_{\text{tot}}[f_{\text{osc}} \cos(\gamma_\mu B_{\text{int}} t + \phi_{\text{ZF}}) e^{-\lambda_1 t} + (1 - f_{\text{osc}}) e^{-\lambda_2 t}], \quad (1)$$

and wTF time spectra with a function with three oscillation frequencies,

$$A(t) = A_{\text{tot}}[f_1 \cos(\gamma_\mu B_1 t + \phi_1) e^{-\lambda_1 t} + f_2 \cos(\gamma_\mu B_2 t + \phi_2) \times e^{-\lambda_2 t} + (1 - f_1 - f_2) \cos(\gamma_\mu B_{\text{ext}} t + \phi_{\text{ext}}) e^{-\lambda_{\text{ext}} t}], \quad (2)$$

where  $f$  and  $B$  represent the volume fraction and the field strength of the oscillation components:  $f_{\text{osc}}, B_{\text{int}}$  for ZF and

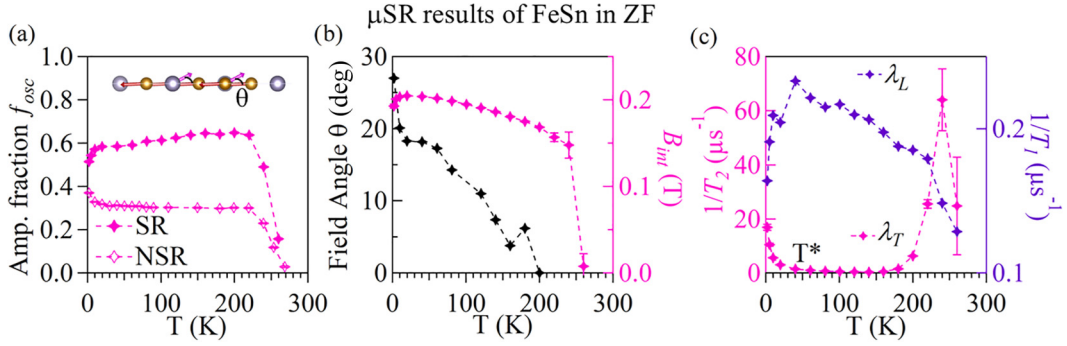


FIG. 5. Fitting results extracted from Eq. (1). (a)  $T$  dependence of the oscillating amplitude fraction  $f_{\text{osc}}$  in both SR and NSR modes. The inset shows the angle  $\theta$  between the muon local field  $B_{\text{int}}$  and the  $ab$  plane. (b)  $T$  dependence of the estimated field angle  $\theta$  and the spontaneous magnetic internal field  $B_{\text{int}}$ . (c)  $T$  dependence of the transverse relaxation rate  $1/T_2$  and the longitudinal relaxation rate  $1/T_1$ .

$f_{1,2}$ ,  $B_{1,2}$  for wTF.  $\lambda_T$  and  $\lambda_{\text{ext}}$  represent the transverse damping rate caused by the finite field distribution at the muon site and  $\lambda_L$  the longitudinal relaxation rate which is also usually denoted as  $1/T_1$ . The oscillating component  $f_{\text{osc}}$  in ZF comes from the spontaneous magnetic internal field  $B_{\text{int}}$ , while the corresponding magnetic components observed in wTF are  $f_1$  and  $f_2$ . As shown later,  $f_{\text{osc}}$  is very close to  $f_1 + f_2 \sim 0.6$ . The remaining nonoscillating component  $(1 - f_{\text{osc}})$  in ZF in Eq. (1) can originate from a paramagnetic/nonmagnetic environment for muon and/or the longitudinal asymmetry component in the magnetically ordered regions known as the 1/3 tail for the case of a powder sample in ZF. Since the present specimens are single-crystalline with the  $ab$  plane randomly aligned, we expect a negligible 1/3 tail component in the ZF-SR mode. In this situation, this  $(1 - f_{\text{osc}}) \sim (1 - f_1 - f_2)$  component should oscillate in wTF at a frequency of the applied external field  $B_{\text{ext}}$ , and this was confirmed in our experiments. The volume fraction  $(1 - f_{\text{osc}})$  can be due to a phase-separated paramagnetic region and/or a fraction of muons located at a high-symmetry site where the local field cancels. This aspect will be discussed later with the simulation of the muon sites and local fields.

In Fig. 5(a), we show the temperature dependence of the fraction of the oscillating signal  $f_{\text{osc}}$  extracted from fitting ZF time spectra in the SR mode with Eq. (1). This figure indicates that  $\sim 40\%$  muons remain in a para/nonmagnetic environment below 240 K. We also show the fraction of the oscillating signal in ZF-NSR mode, which is roughly half of the fraction seen in ZF-SR. This further confirms that the local field at the high-field muon site is pointing nearly perpendicular to the  $c$  axis within the  $ab$  plane. However, in a close inspection of the amplitudes in the ZF-SR and ZF-NSR modes in Fig. 5(a), we find that this 2:1 ratio changes below  $T \sim 150$  K. Such change can be expected if the local field at the high-field site exhibits canting toward the  $c$ -axis direction, as the oscillating amplitude follows  $f_{\text{osc}}(\theta) \sim \cos^2\theta$  with the canting angle  $\theta$  illustrated in the inset of Fig. 5(a). The canting angle estimated from the amplitude ratio is shown in Fig. 5(b). In Fig. 5(b), we also show the temperature dependence of the spontaneous magnetic internal field  $B_{\text{int}}$  at the high-field muon site. The  $T$  dependence of the frequency exhibits a departure at low temperatures from the standard behavior expected for a sublattice magnetization of an antiferromagnet.

Figure 5(c) shows the transverse relaxation rate  $1/T_2$  of the precessing component and the longitudinal relaxation rate  $1/T_1$  observed in the ZF-SR mode. The increase in  $1/T_2$  below  $T \sim 50$  K (denoted as  $T^*$ ) suggests some anomaly, which will be discussed later with  $\mu$ SR results in LF and the corresponding anomaly found in magnetic susceptibility. In contrast, the  $1/T_2$  peak at  $T \sim 250$  K is not associated with any corresponding signature of susceptibility and therefore can be attributed to the effect of muon diffusion.

### 3. Double-peak spectra in wTF

In our wTF measurements, we notice that the high-field muon site with  $B_{\text{int}}$  in ZF generates oscillating signals with two split frequencies close to  $B_{\text{int}}$ , as shown in Figs. 4(e) and 4(f). We denote these fields as  $B_1$  and  $B_2$  and their signal amplitude fractions as  $f_1$  and  $f_2$ , and show the temperature dependencies in Figs. 6(a) and 6(b). In wTF = 10 mT,  $B_1$  and  $B_2$  are very close to the ZF spontaneous magnetic field  $B_{\text{int}}$  plus or minus 10 mT, and their fractions are equal to each other  $\sim 0.3$  independent of temperature below  $T \sim 250$  K. In Fig. 6(c), we show how these two frequencies depend on the varying transverse external field  $B_{\text{ext}}$  at  $T = 60$  K. This figure demonstrates the linear relationships between  $B_1$  and  $B_2$  on  $B_{\text{ext}}$ . In the wTF geometry, the single crystals are aligned by their  $c$  axis, while directions of  $a$  or  $b$  axes are randomly oriented within the  $ab$  plane. The external TF field was applied perpendicular to the  $c$  axis. The local field observed in this configuration should be a vector sum of the internal field and the external field,  $\vec{B}_{\text{int}} + \vec{B}_{\text{ext}}$ , as illustrated in Fig. 6(d), which shows a top view of the vector sum. The angular dependence of the local field strength  $\vec{B}$  seen by the muons can be derived from  $B^2 = B_{\text{int}}^2 + B_{\text{ext}}^2 + 2B_{\text{int}}B_{\text{ext}}\cos(\alpha)$ , where  $\alpha$  is the angle between  $B_{\text{int}}$  and  $B_{\text{ext}}$ . By assuming  $B_{\text{int}} = 0.2$  T, we plot the angular dependence of field  $B$ , in Fig. 6(e). The probability of fields seen by muons,  $\frac{\partial\alpha}{\partial B}$  in Fig. 6(f), can then be used to describe the field distribution in the time spectra. This is consistent with the two peaks of  $B_1$  and  $B_2$  observed in the FFT of the wTF spectra in Figs. 4(e) and 4(f).

### 4. Low temperature anomaly and dynamic responses in LF

To further study the anomalies found in ZF at low temperatures, as described in Sec. III A 2, we performed ZF and LF

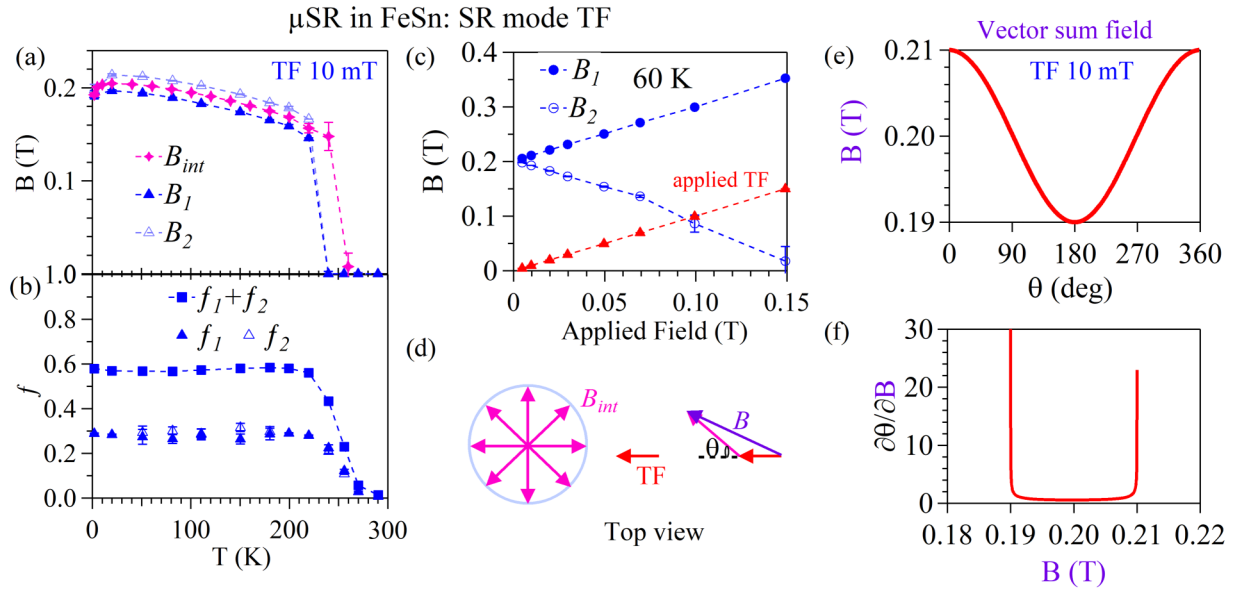


FIG. 6. (a)  $T$  dependence of the magnetic fields. (b)  $T$  dependence of the volume fraction under TF 100 G. (c) Transverse field dependence of the observed frequencies,  $B_{1,2}$  of FeSn at 60 K. (d) Top view of the Fe magnetic moment in the  $ab$  plane,  $B_{int}$ , external field TF was applied within the plane, and the vector sum,  $B$ , of the internal and external fields. (e) The simulated angular dependence of the field strength. (f) The probability of the field seen by muons, as described in the main text.

$\mu$ SR measurements in the NSR mode, where external fields were applied parallel to the kagome plane and the initial muon spin. Figure 7(a) shows time spectra at selected temperatures under LF-0.4 T. In low LF with 10 mT and 20 mT, we fit the time spectra with Eq. (1) as used in ZF. We fit the LF-0.4 T spectra with a simple exponential relaxing function:  $A(t) = A_{tot}e^{-\lambda_{L,LF}t}$  in the time range of 0.5–10  $\mu$ s. In Fig. 7(b), we show the relaxation rate observed in ZF and LF under NSR configuration. A clear  $1/T_1$  peak was observed at  $T \sim 50$  K both in ZF and LF measurements, suggesting that dynamic spin fluctuations taking place well below the antiferromagnetic ordering temperature 376 K of FeSn. The change of the time spectra in Fig. 7(a) involves at least half of the full amplitude, which indicates that this is a change taking place in the bulk volume fraction, ruling out the possibility of an effect originating from a minority impurity phase. Together with the reorientation and broadening of the static internal

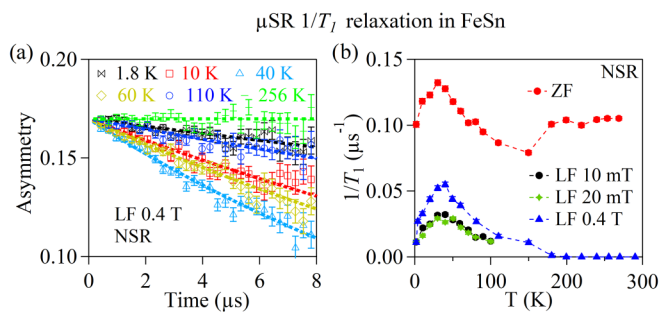


FIG. 7. (a) LF-0.2 T time spectra at selected temperatures in NSR mode. (b) Temperature dependence of the longitudinal relaxation rate,  $1/T_1$ , in ZF, LF-10 mT, LF-20 mT, and LF-0.4 T. A relaxation peak in  $1/T_1$  is robustly seen below 50 K.

field discussed in Sec. III A 2, these anomalies detected by  $\mu$ SR at low temperatures suggest the existence of a magnetic instability in bulk FeSn.

## B. Magnetic susceptibility and resistivity of FeSn

In previous transport studies on FeSn, no clear sign of any anomaly below 50 K was reported [41,42,44,45,77,80–82]. To search for a possible signature corresponding to the low-temperature anomaly found in our  $\mu$ SR results, we performed resistivity measurements. As shown in Fig. 8(a), no clear signature of any anomaly was found in resistivity and its temperature derivatives.

We also performed dc- and ac-magnetic susceptibility measurements. Figure 8(b) shows the dc susceptibility measured under external field  $H$  of 0.1 T. The results with  $H$  along the  $c$  axis correspond to the perpendicular susceptibility, while  $H$  perpendicular to the  $c$  axis includes an average of 50% parallel and 50% perpendicular susceptibility in the absence of spin flopping. The observed amplitude ratio of these two configurations is consistent with the expectation of an antiferromagnet with a transition temperature of  $\sim 376$  K. In addition to this antiferromagnetic transition, a small kink at  $T \sim 50$  K was also observed in the ZFC mode, which was further pronounced in the FC mode. Upon closely examining the previously reported temperature dependence of the derivative of dc susceptibility in Ref. [44], we found a similar kink corresponding to this anomaly.

Figure 8(c) shows the results of our ac susceptibility measurements at several frequencies with the driving ac field both parallel and perpendicular to the  $c$  axis. A clear increase in the imaginary part  $\chi''$  was observed below 50 K for both driving field directions in zero external field and the 0.1 T external field applied along the  $c$  axis and the  $ab$  plane. This

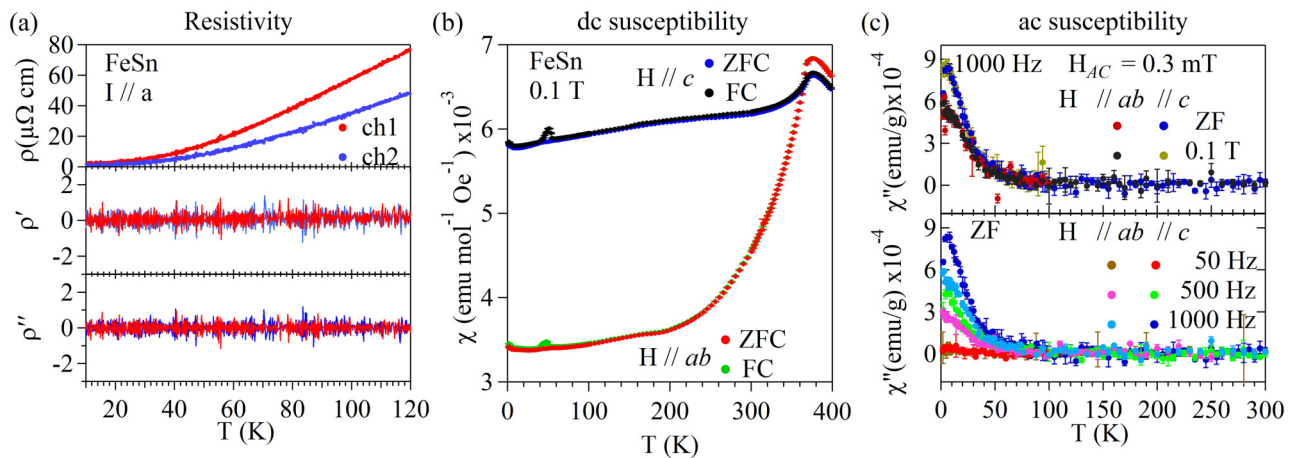


FIG. 8. (a)  $T$  dependence of the resistivity and its derivatives in two independent channel setups ch1 and ch2 on the same crystal. Current,  $I$ , was applied along a direction. (b) dc susceptibility results of FeSn under 1 kG external field along the  $c$  axis and  $ab$  plane. In addition to the antiferromagnetic transition at  $\sim 376$  K, a small kink around  $\sim 50$  K was observed in the ZFC mode, which was further enhanced in the FC mode. (c) Frequency and field dependence of ac susceptibility in FeSn with ac amplitude of 3 G. Additional dc field was applied both along the  $c$  axis and  $ab$  plane. The observed imaginary part  $\chi''$  is independent with the field while exhibiting a clear increase below 50 K.

result indicates a development of magnetic dynamics at low temperatures below  $T \sim 50$  K. These susceptibility results correspond very well to the anomalies observed in  $1/T_1$  and  $1/T_2$  by  $\mu$ SR. Note that  $1/T_1$  and  $\chi''$  both reflect dynamic spin fluctuations. This excellent correspondence indicates that the  $\mu$ SR anomalies observed at and below  $T \sim 50$  K are most likely due to the intrinsic property of FeSn rather than a phenomenon caused specifically by the existence of a positive muon in the material.

### C. Scanning tunneling microscopy and spectroscopy of FeSn

We also performed STM and scanning tunneling spectroscopy (STS) studies on the bulk FeSn. Our main motivation came from a previous report of STM studies on a thin film of FeSn, which included a signature of spontaneous trimer formation of the kagome lattice at low temperatures [48], reminiscent of spin Peierls transition in low-dimensional systems. Trimer formation might explain the  $T \sim 50$  K signatures observed by  $\mu$ SR and magnetic susceptibility.

Figure 9(a) shows a large area topography of the cleaved FeSn surface. We see two distinct surface terminations, Sn<sub>2</sub> and Fe<sub>3</sub>Sn, the former being the predominant surface termination. Figures 9(b) and 9(c) show atomically resolved STM topographies of the two surfaces. For the Sn<sub>2</sub> surface, we can resolve each Sn atom, which shows a clear honeycomb lattice structure. For the Fe<sub>3</sub>Sn kagome structure, however, the individual atoms are not resolved. A lattice model is overlaid on both topographies. Scanning tunneling spectroscopy shows a peak around  $-50$  mV for the Sn<sub>2</sub> termination which is not present for the Fe<sub>3</sub>Sn kagome termination [83,84]. To investigate the possibility of any broken symmetry visible to STM at low temperatures, we performed spectroscopic imaging experiments on both surfaces. Shown in Fig. 9(e) is a large area topography of the Sn<sub>2</sub> surface that has several defects. Simultaneously obtained dI/dV maps at two different energies are shown in Figs. 9(f) ( $-100$  mV) and 9(g) ( $-50$  mV). The

corresponding FFT magnitudes are shown in Figs. 9(h) and 9(i). Our spectroscopic imaging experiments reveal no clear evidence for additional Bragg spots that have been seen in FeSn thin films [48] and no evidence for rotational symmetry breaking.

A previous STM study on the FeSn film, which reported a signature of trimer formation, presented dI/dV signal from two adjacent triangles in Fe<sub>3</sub>Sn termination. We generated a similar plot and show the results in Fig. 10 with the dI/dV map for the sample bias voltages of 60 mV in (a) and  $-200$  mV in (b), and the averaged dI/dV signal in (c) from several locations of A, B, and C, as illustrated in (b). Unlike a previous report on a thin film FeSn sample that exhibited clear differences in the signals between A and B, our results from a bulk single crystal of FeSn showed no difference between A and B, indicating that there is no signature of trimer formation in our STM results. Thus, our initial attempt to find signatures of possible phase transition results in a negative answer. However, since STM gives selective information on the surface, this result does not necessarily represent the situation in bulk FeSn. Therefore, trimer formation has not yet been completely ruled out as a possible explanation of the  $T \sim 50$  K anomaly observed by the two bulk sensitive probes,  $\mu$ SR and magnetic susceptibility. We will continue STM studies at higher temperatures and start high-resolution x-ray studies to further seek the possible origin of the 50 K anomaly.

### D. Muon site and local fields in FeSn

To better understand the origin of the 40% paramagnetic-like volume in FeSn, we turn to investigate the possible muon sites. The  $\mu$ SR results in ZF and wTF described above indicate that the static local field at the magnetic muon stopping site points perpendicular to the  $c$  axis in the antiferromagnetic state, which provides a strong restriction on the muon stopping site in the planar spin structure. Generally, the main characteristics of the coupling between the dipolar moment of

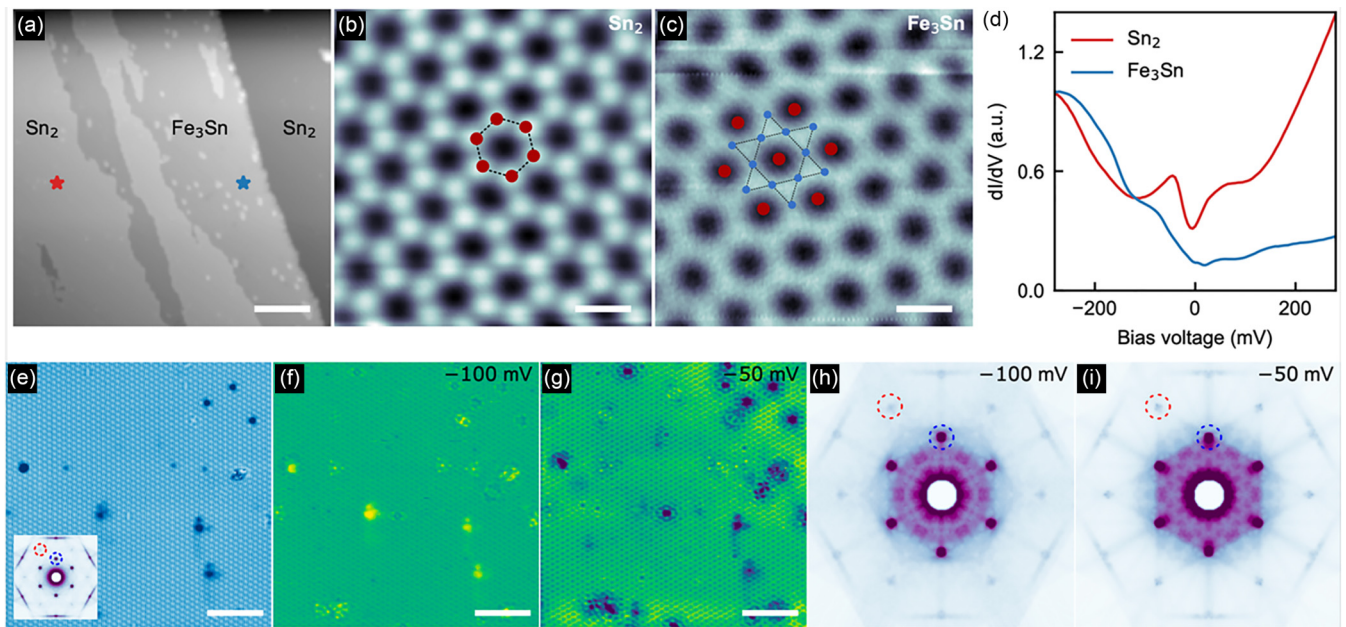


FIG. 9. STM on the bulk cleaved surface of FeSn. (a) STM topography of the cleaved surface showing  $\text{Sn}_2$  and  $\text{Fe}_3\text{Sn}$  termination layers. (b) Constant current mode topography of the  $\text{Sn}_2$  surface showing a honeycomb structure where individual Sn atoms can be seen. (c) Constant current topography of the  $\text{Fe}_3\text{Sn}$  kagome termination with a lattice model overlaid on top. Red atoms are Sn and blue atoms are Fe. (d) Scanning tunneling spectroscopy on the surfaces of  $\text{Sn}_2$  and  $\text{Fe}_3\text{Sn}$ , indicated in (a) and (e). Large area constant current mode topography of the  $\text{Sn}_2$  surface showing different kinds of defects. The inset shows the FFT of the topography. (f), (g) Spatial map of differential conductance,  $dI/dV$  at energies  $-100$  mV and  $-50$  mV. (h), (i) The corresponding FFTs of the  $dI/dV$  map as shown in (f) and (g). STM setpoint conditions: (a)  $-600$  mV,  $100$  pA; (b)  $50$  mV,  $1.9$  nA; (c)  $-200$  mV,  $1.9$  nA; (d)  $-300$  mV,  $500$  pA; (e)  $-100$  mV,  $200$  pA; (f)  $-100$  mV,  $200$  pA; (g)  $-50$  mV,  $200$  pA. Scale bars: (a)  $10$  nm; (b), (c)  $0.5$  nm; (e)–(g)  $5$  nm.

Fe and the muon are the isotropic hyperfine coupling and the dipolar field coupling.

In Fig. 11, we show the total electron energy of possible muon stopping sites, starting from a high symmetry point and then moving along the  $c$  axis. This calculation and stability/symmetry analysis reveal that two plausible muon stopping sites are the lowest electrical potential site,  $\mu_1 = (1/3, 2/3, 0)$ , and the second lowest site,  $\mu_2 = (0, 0, 1/2)$ , as marked by red and blue dots. The latter  $\mu_2$  site is located at the high symmetry point, where the local field vanishes in the

planar spin structure. This site is the strongest candidate for the field-cancelling site, where 40% of the implanted muons reside. The former  $\mu_1$  site exists in the kagome plane, and our dipolar field calculation indicates a local field strength of  $0.9352$  T within the  $ab$  plane for the planar magnetic structure with an Fe moment size of  $1.85 \mu_B$  as determined in Ref. [44] at  $100$  K. This dipolar field strength is much larger than what we observed:  $\sim 0.2$  T. Note that FeSn is metallic and the muon hyperfine contact field is not negligible. Previous DFT calculations and muon studies in pure bcc Fe crystal indicate

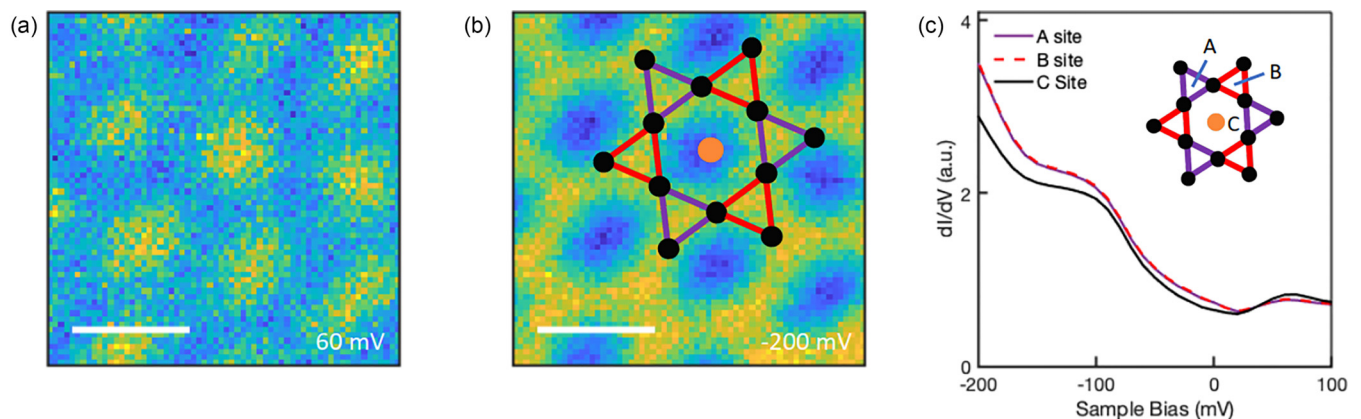


FIG. 10. STS results of the  $dI/dV$  from the  $\text{Fe}_3\text{Sn}$  termination of a cleaved bulk single crystal of FeSn. (a)  $dI/dV$  map with the bias voltage of  $60$  meV. (b) with  $-200$  meV and (c) bias voltage dependence of the  $dI/dV$  signal from A, B, and C locations as illustrated in (b). Set point conditions for (a)–(c):  $300$  mV,  $700$  pA. In contrast to a previous report on STS of a thin film specimen of FeSn [48], we found no difference between the signal from A and B, which rules out the formation of a trimer state.

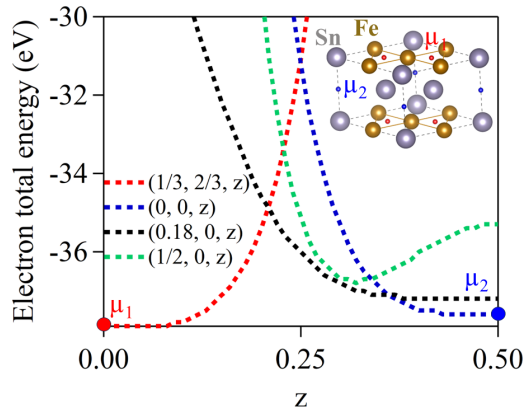


FIG. 11. The electron total energy of calculated muon stopping sites, starting from a high symmetry point and moving along the  $c$  direction. Inset shows the two plausible muon stopping sites  $\mu_1$  and  $\mu_2$ , marked as red and blue dots. The  $\mu_1$  site sits in the center of three Fe atoms while the  $\mu_2$  site sits in the middle of two Sn atoms between kagome layers.

a large hyperfine field  $\sim -1.11$  T [85,86]. The  $\mu$ -Fe distance in bcc Fe is about  $1.587$  Å, which is close to the value for  $\mu_1$  ( $1.53$  Å) in FeSn. By including this hyperfine field in our dipolar calculation, the estimated local field becomes  $0.175$  T, which agrees fairly well with our ZF- $\mu$ SR observation of  $0.195$  T at  $100$  K. We can alternatively estimate the hyperfine field from the observed results in FeSn to be  $\sim -1.07$  T.

We further studied the effect of the reorientation of Fe moments to understand the observed field canted toward the  $c$  axis as shown in Fig. 5(b). Assuming the Fe spins reorient out of plane while maintaining the antiferromagnetic arrangement between the kagome layers, we found that a  $2^\circ$  rotation of Fe spins toward the  $c$  axis would result in a field canted angle  $\theta \sim 32^\circ$ .

### E. $\mu$ SR in $\text{Fe}_{0.89}\text{Co}_{0.11}\text{Sn}$

To further examine the origin of the 40% volume fraction without static internal field (except for nuclear dipolar fields) observed in FeSn, we turned to Co-doped  $\text{Fe}_{0.89}\text{Co}_{0.11}\text{Sn}$ . In Figs. 12(a) and 12(b), we show the time spectra of  $\text{Fe}_{0.89}\text{Co}_{0.11}\text{Sn}$  in ZF-SR at selected temperatures and TF  $10$  mT at  $300$  K. A fast-damped oscillation at  $300$  K in ZF was observed, indicating behaviours expected for a full volume of static magnetic order. With decreasing temperatures, oscillations seen at  $300$  K turn into a fast damping signal, which may be due to the reorientation of Fe moments from a planar magnetic structure to a tilted complex magnetic structure [45,77]. We present the temperature dependence of the longitudinal relaxation rate in the inset of Fig. 12(b). A peak in the  $1/T_1$  rate was observed at about  $200$  K, corresponding to the magnetic transition as seen in the phase diagram in Fig. 1.

The time spectra at TF  $10$  mT in  $\text{Fe}_{0.89}\text{Co}_{0.11}\text{Sn}$  in Fig. 12(b) do not show any oscillations at the applied TF. This implies that there is no paramagnetic or nonmagnetic volume, and the full  $100\%$  volume is in a magnetically ordered state at  $300$  K. This absence of phase separation between magnetically ordered and paramagnetic volumes in the Co  $11\%$  compound strongly suggests that the nonoscillating

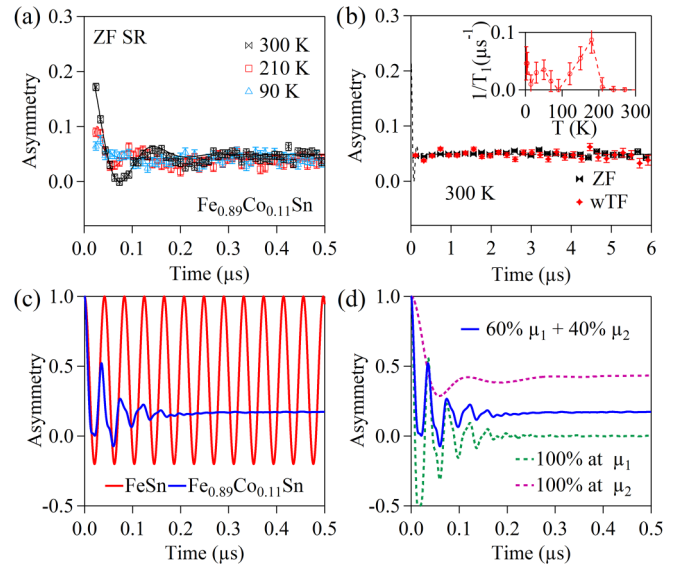


FIG. 12. (a) ZF  $\mu$ SR spectra within  $0.5$   $\mu\text{s}$  at selected temperatures. The oscillation seen at  $300$  K was smeared out by the fast  $1/T_2$  rate with a decrease in temperature. (b) wTF  $10$  mT time spectra in the long time window, which shows no oscillation, indicating a fully ordered magnetic state at  $300$  K. The inset shows the temperature-dependent small  $1/T_1$  relaxation rate, which exhibits a transition at around  $200$  K. (c) Simulation of ZF time spectra for FeSn and  $\text{Fe}_{0.89}\text{Co}_{0.11}\text{Sn}$ . (d) ZF time spectra of  $\text{Fe}_{0.89}\text{Co}_{0.11}\text{Sn}$  with different mixture volume of suggested muon sites.

signal with  $40\%$  volume fraction observed in FeSn is not due to phase separation, although the situation in the Co  $11\%$  compound does not directly represent that in pure FeSn.

We simulated the ZF time spectra of  $\text{Fe}_{0.89}\text{Co}_{0.11}\text{Sn}$  based on the dipolar and hyperfine fields by randomly replacing  $11\%$  Fe atoms with nonmagnetic Co atoms while retaining the planar magnetic structure of FeSn. Although the hyperfine field may vary with different concentrations and materials, we used the hyperfine field of  $\sim -1.11$  T in our simulation as the simplest approximation. Figure 12(c) shows the ZF time spectra of  $\text{Fe}_{0.89}\text{Co}_{0.11}\text{Sn}$  and FeSn, generated by assuming a volume ratio of  $60\% : 40\%$  for  $\mu_1$  and  $\mu_2$  sites. The depolarization in  $\text{Fe}_{0.89}\text{Co}_{0.11}\text{Sn}$  increases as compared to that in FeSn, which is consistent with our experimental results.

We further generated hypothetical ZF time spectra for  $\text{Fe}_{0.89}\text{Co}_{0.11}\text{Sn}$ , as shown in Fig. 12(d), assuming muon stopping sites to be exclusively either  $\mu_1$  or  $\mu_2$  sites. The simulated spectrum with a  $100\%$   $\mu_2$  site (purple broken line) shows fast depolarization followed by a  $1/3$  tail. The field-absent phenomenon disappears because the local high symmetry was broken due to the disorder caused by the (Fe, Co) substitutions. This simulation provides further support to our argument that the  $40\%$  field-absent volume fraction in FeSn is due to internal field cancellation at the high-symmetry muon site  $\mu_2$  rather than the effect of phase separation.

### F. $\mu$ SR in $\text{Fe}_{0.2}\text{Co}_{0.8}\text{Sn}$

#### 1. ZF and LF $\mu$ SR results

As shown in the phase diagram in Fig. 1, Co substitutions above  $50\%$  lead to a spin glass state. In this region, we

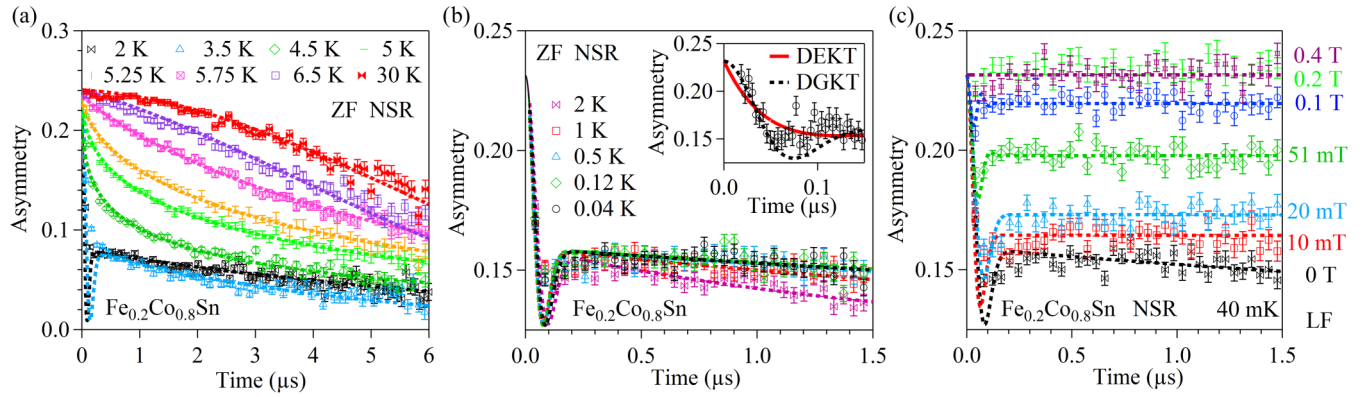


FIG. 13. Dashed lines are fitting results, as described in the main text. (a) ZF- $\mu$ SR time spectra of  $\text{Fe}_{0.2}\text{Co}_{0.8}\text{Sn}$  at selected temperature above 2 K. (b) ZF- $\mu$ SR time spectra with temperatures below 2 K. Inset: The front end of the 40 mK time spectra with the fitting of both exponential relaxation and Gaussian relaxation. (c) LF- $\mu$ SR spectra at 40 mK with fields up to 0.4 T. The relaxation rate was quickly decoupled and fully decoupled above 0.2 T.

performed  $\mu$ SR studies of  $\text{Fe}_{0.2}\text{Co}_{0.8}\text{Sn}$  with the spin freezing temperature  $T_g \sim 3.5$  K [45]. Figure 13(a) shows time spectra of ZF NSR measurements taken at M20 at  $T \geq 2$  K with the dashed lines representing fits to Eq. (3). At very high temperatures, such as  $T = 30$  K, the effect of the local field from Fe moments is eliminated by the fast spin fluctuations. Here, muon depolarization is caused by nuclear dipolar fields (mainly from Co nuclei in the present case), and we observed a Gaussian Kubo-Toyabe function  $g_z(\Delta, t)$  for static nuclear fields with  $\Delta(30 \text{ K}) = 0.121 \mu\text{s}^{-1}$ . With a decrease in temperature, the spectra changed into a product of the dynamic relaxation because of the fluctuating local field from Fe and the above-mentioned static Kubo-Toyabe function. Upon approaching  $T_g$ , the dynamic depolarization rate rapidly increases, suggesting the slowing down of the Fe moments. In general, line shapes for dynamic relaxation are given by stretched exponential functions,  $e^{-(\lambda t)^\beta}$ , with the stretching power  $\beta$  depending on the field distributions and fluctuation timescales. For example,  $\beta = 1/2$  can be expected for diluted and random magnetic systems in the narrowing limit [78,87]. The present system has relatively dense Fe moments, as suggested by the Gaussian initial damping of the time spectrum at  $T \rightarrow 0$  shown in the inset of Fig. 13(b). In this case, a simple exponential decay with  $\beta = 1$  is expected for the dynamic relaxation function. The observed time spectra agree well with this expectation, as shown by dotted lines in Fig. 13.

With further decreases in temperatures below  $T_g$ , the polarization rapidly drops to  $\sim 1/3$  of its initial value followed by the 1/3 tail, which slowly relaxes in the longer times, as expected for coexisting static and dynamic random local fields. We used a phenomenological model to extract the static and dynamic effects of local fields using a product function of the static response of the Kubo-Toyabe function with dynamic simple exponential decay. The observed 1/3 tail relaxes slower at 2 K as compared to 3.5 K as shown in Fig. 13(a), which indicates a decrease of dynamic relaxation in lower temperatures. To characterize the temperature dependence of the dynamic relaxation, we performed additional measurements on the same crystals down to 40 mK using the M15 beamline. The time spectra observed in the ZF-NSR mode in Fig. 13(b) demonstrate that the 1/3 tail relaxes even slower at lower temperatures. The early-time relaxation of the

40 mK data, as shown in the inset, was better described by a Gaussian relaxation (DGKT) rather than an exponential relaxation (DEKT). This indicates that the local field distribution is close to Gaussian, as expected in relatively dense magnetic systems.

We also performed LF  $\mu$ SR measurements, where the external field is applied in the direction of the initial muon spin. A static signal will be nearly fully decoupled by an applied field that is a few times larger than the static internal field measured in zero field. In contrast, if the relaxation of the ZF  $\mu$ SR signal is due to dynamics, the signal will not be decoupled by an applied field of this magnitude. Figure 13(c) shows the LF results at 40 mK. The 1/3 tail becomes nearly flat (nonrelaxing) with a small LF of only 10 mT, indicating that the dynamic effect is negligible. We also observed a gradual decoupling of fast relaxation with increasing applied longitudinal fields and a nearly complete restoration of asymmetry with LF  $\sim 0.2$  T, consistent with the initial ZF relaxation shown in the inset of Fig. 13(b).

We note that the background signal from the sample holder and surrounding sample environment in the dilution cryostat gives a significant contribution (up to  $\sim 40\%$  of the signal amplitude) to the data taken at M15. The slow but finite decay of the flat signal observed in ZF at 40 mK shown in Fig. 13(b) is due to the effect from the nuclear dipolar field in the background signal, which was eliminated by applying a small external LF of 10 mT. To fit the signal from the sample, we assumed the phenomenological function  $G_{\text{SKT}}(\Delta, t)$  multiplied by dynamical simple exponential decay rate  $1/T_1$  as

$$A(t) = A_{\text{KT}} G_{\text{SKT}}(\Delta, t) e^{-\frac{t}{T_1}}, \quad (3)$$

where

$$G_{\text{SKT}}(\Delta, t) = \frac{1}{3} + \frac{2}{3}(1 - (\Delta t)^\alpha) e^{-(\Delta t)^\alpha/\alpha}, \quad (4)$$

with  $\alpha = 2$  for the Gaussian Kubo-Toyabe function:

$$g_z(\Delta, t) = \frac{1}{3} + \frac{2}{3}(1 - (\Delta t)^2) e^{-(\Delta t)^2/2}. \quad (5)$$

The background signal in the M15 data was included by an additional term  $e^{-(\lambda_{\text{bg}} t)}$  in the fitting process. Since the M20 apparatus is an ultralow background setup, we compared

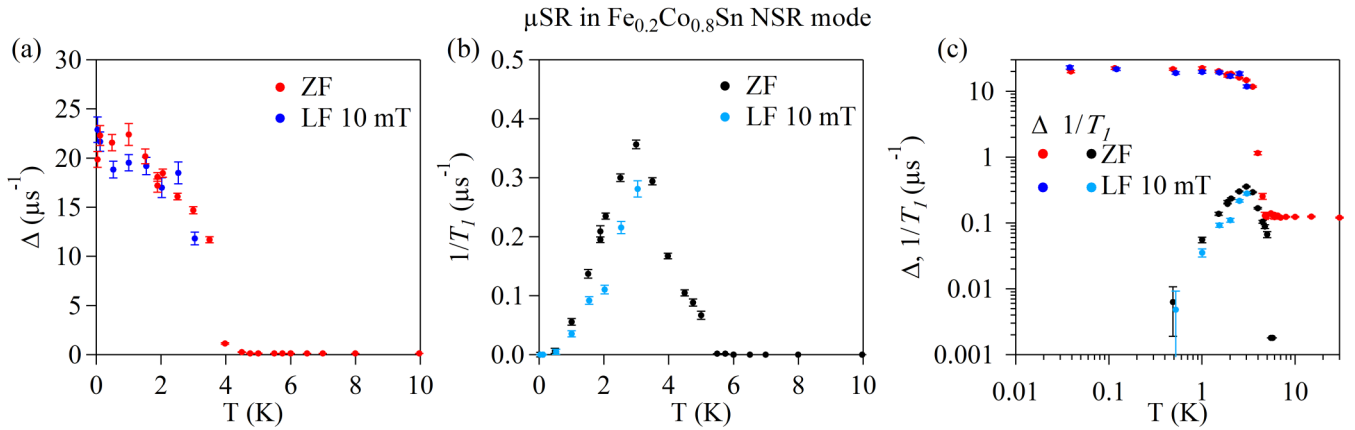


FIG. 14.  $T$  dependence of the (a) static relaxation rate  $\Delta$  and (b) dynamic relaxation rate,  $1/T_1$  at ZF/LF-100G in NSR mode. (c) Plot of  $\Delta$  and  $1/T_1$  together on a logarithmic scale.

the M15 data and M20 data taken at the same temperatures to correctly obtain the sample volume fraction and its slow fluctuation rate. Figure 14 shows the temperature dependence of the relaxation rate,  $\Delta$ , and the low temperature dynamical fluctuation rate,  $1/T_1$ , thus derived from this fit.

In spin glass systems, the relaxation function in ZF around  $T_g$  often exhibits complicated line shapes, which are difficult to parametrize with a simple formula. Given this, we adopted an approach to use the general Kubo-Toyabe function, connecting smoothly crossing  $T_g$ . In the region at temperatures below  $T_g$ , the stretched power parameter  $\alpha$  was set to 2 to account for the observed early Gaussian decay. The static relaxation rate,  $\Delta$ , which reflects the width of the static internal field distribution, can be viewed as the order parameter. The Gaussian relaxation rate at 40 mK gives an estimated static local field as  $\Delta/\gamma\mu = 20.28/(2\pi \times 135.5) = 23.8$  mT. We note that the minimum of the Kubo-Toyabe function does not agree perfectly with our data, as shown in Fig. 13, which might mean that the true field distribution is somewhat more complicated. The dynamic relaxation rate,  $1/T_1$ , peaks around  $T_g$  and decreases to  $0.001(4) \mu\text{s}^{-1}$  at 40 mK in ZF. We took additional LF 10 mT measurements to study the dynamic relaxation rate. The relaxation rates  $1/T_1$  in LF 10 mT decrease with temperature and becomes essentially zero below our detection limit at  $T = 40$  mK. These results indicate that the dynamic spin fluctuations are frozen and the spin system becomes completely static. These behaviors are similar to previously known results in the canonical dilute-alloy spin glasses AuFe and CuMn [78], while distinctly different from the persistent spin dynamics observed in several geometrically frustrated spin systems at  $T \rightarrow 0$ .

## 2. Fe moment size estimated from comparisons between the observed spectra and the dipolar field simulation

To estimate the frozen static moment size of Fe, we performed simulations of the dipolar field by assuming two muon sites with a volume ratio of 60%: 40% for  $\mu_1$  and  $\mu_2$  sites. The dipolar fields can be simulated for randomly allocated and oriented magnetic Fe atoms. Subsequently, we compared our simulations with the experimental ZF time spectra at 40 mK

to estimate the effective moment size. Figure 15(a) compares the simulated time spectra obtained for various Fe moment sizes with the experimental data and its fitting using Eq. (3). From this comparison, we obtain an effective moment size of  $0.45(0.05) \mu_B$ . Note that the hyperfine field is not included in this argument, which gives a significant uncertainty to this estimate. Figure 15(b) shows the results of our dc susceptibility measurements under an external field applied of 0.1 T. We fit the results with the Curie-Weiss law above 10 K, as shown by the solid blue line in Fig. 15(b). The ordered moment size  $\sim 0.45 \mu_B$  is nearly half of the effective moment  $0.81 \mu_B$  obtained from the magnetic susceptibility above  $T_g$ . Such reduction is commonly seen in many spin-glass systems. Figure 15(c) shows the real part ( $\chi'$ ) results of our ac susceptibility measurements at several frequencies with an excitation field of 0.3 mT after cooling the sample in the zero field. It exhibits the anomaly at  $\sim 3.5$  K for 1 Hz and was found to be frequency dependent. The peak position shifts toward higher  $T$  with increasing frequency, consistent with a glass transition and  $T_g \sim 3.5$  K.

## IV. DISCUSSIONS, CONCLUSIONS, AND OUTLOOK

### A. Intrinsic versus muon-specific anomalies in FeSn

In the present  $\mu\text{SR}$  studies of FeSn, we found four notable features: (i) the  $T \sim 50$  K anomaly of  $1/T_1$  and  $1/T_2$  in Figs. 5 and 7; (ii) a signature of reorientation of local field direction toward  $c$ -axis direction at  $T < 100$  K and anomaly of ZF precession frequency at low temperatures in Figs. 5(a) and 5(b); (iii) existence of the field canceling muon site with  $\sim 40$  % volume fraction; and (iv) anomaly of  $1/T_2$  at  $T \sim 250$  K in Fig. 5(c), very slow relaxation in nearly full amplitude in ZF at  $T > 260$  K in Fig. 4(a), and the full amplitude oscillation at the applied wTF frequency at  $T = 270$  K in Figs. 4(d) and 4(f). Among them, (i) is clearly due to the intrinsic features of FeSn, as it is associated with the corresponding anomalies in the ac and dc magnetic susceptibility shown in Figs. 8(b) and 8(c). Currently, the origin of this anomaly has not yet been identified. In an isostructural and ferromagnetic FeGe, a CDW transition is observed within the antiferromagnetically ordered state, as identified by the associated anomalies in

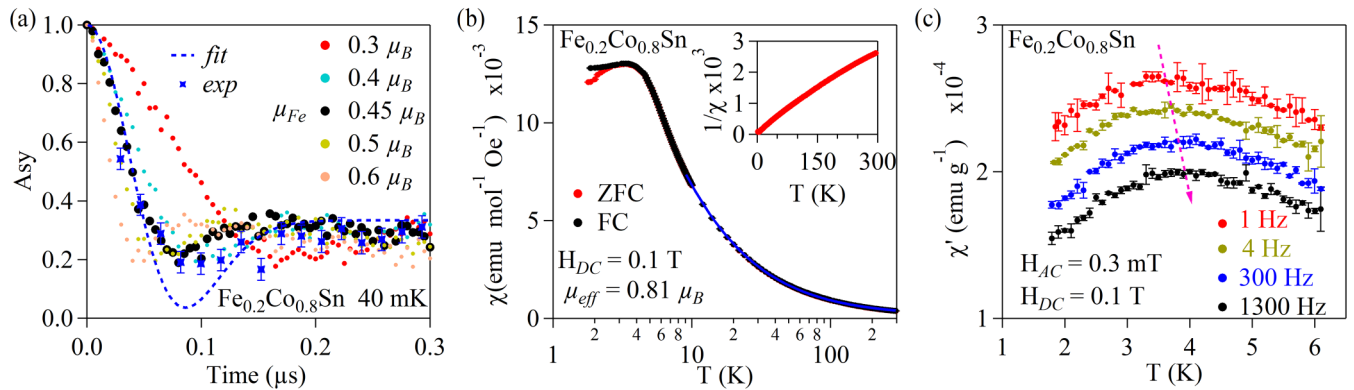


FIG. 15. (a) ZF time spectra with various Fe moment sizes from dipolar field simulations. The blue line is the fitting result obtained from the KT function, blue stars represent the experimental data points. Other solid circle lines show the simulated time spectra with various moment sizes. The best fit was obtained with  $\mu_{Fe} \sim 0.45 \mu_B$ . (b)  $T$  dependence of dc susceptibility of  $\text{Fe}_{0.2}\text{Co}_{0.8}\text{Sn}$ . The effective paramagnetic moment size, obtained from a Curie-Weiss fit (solid line), was found to be  $0.81 \mu_B$ . The inset shows the  $T$  dependence of the inverse of susceptibility. (c)  $T$  dependence of ac susceptibility. A pink arrow is a guide for the eye to show the frequency dependence of  $T_g$ . Offsets of the vertical axis were used in displaying data of 300 Hz, 4 Hz, and 1 Hz for a better view of the frequency dependence.

the  $T$  derivative of resistivity [74] and structural x-ray measurements [88]. In the present case of FeSn, no resistivity anomaly was found, as shown in Fig. 8(a), and no structural anomaly has been reported in neutron studies [43]. Although the trimerization symmetry breaking on the Fe kagome plane was detected by a recent STM study of thin film FeSn at  $\sim 4.5$  K [48], our STM results on cleaved bulk sample reveal no clear evidence for such rotational symmetry breaking as discussed in Sec. III B. To explore CDW, trimerization, and other possibilities, we are planning further studies of STM and high-resolution x-ray scattering on FeSn.

Presently, it is not possible to unambiguously determine whether feature (ii) is due to the intrinsic behavior of FeSn or phenomena related to muon-specific features, such as muon site change, or both intrinsic and muon-specific phenomena. Here we would point out that very similar anomalies corresponding to features (i) and (ii) have been observed in  $\mu\text{SR}$  measurements in planar antiferromagnetic systems CrSBr [89], having ferromagnetically correlated Cr moments in plane, and antiferromagnetic  $\text{RMn}_6\text{Sn}_6$  [90] with rare earth elements  $R = \text{Y}$  and  $\text{Tb}$ , having ferromagnetically aligned Mn moments on kagome planes. It would be very interesting to perform further studies to seek if these common behaviors are due to the physics of layered metallic antiferromagnets with ferromagnetically correlated moments on kagome/triangular lattices and to identify if some muon specific feature is related or not to these observations.

The field canceling site (iii) is the muon-specific phenomenon. In addition to the implication given by the 11% Co-doped FeSn described in the present paper, we draw attention to earlier Moessbauer effect studies on FeSn [76,91–93], which found responses from fully ordered volume below  $T_N = 376$  K, without any evidence of phase separation. The 250 K anomaly (iv) is also a muon-specific result since no corresponding anomaly was seen in dc- and ac-magnetic susceptibility in Fig. 8 and the Moessbauer effect signal in the ordered state around  $T \sim 250$  K. Therefore, we ascribe the 250 K anomaly to muon delocalization/diffusion between the high-field  $\mu_1$  and field-cancelling sites  $\mu_2$  shown in Fig. 11.

## B. Classical spin glass behavior in $\text{Fe}_{0.2}\text{Co}_{0.8}\text{Sn}$

In insulating kagome spin systems with antiferromagnetic nearest-neighbor interactions, such as  $\text{SrCr}_8\text{Ga}_4\text{O}_{19}$  (SCGO) [94],  $\text{KCr}_3\text{OH}_6(\text{SO}_4)_2$  (Cr jarosite) [95], and  $(\text{Cu}_x\text{Zn}_{1-x})_3\text{V}_2\text{O}_7(\text{OH})_2 \cdot 2\text{H}_2\text{O}$  (Volborthite) [96], geometrical frustrations lead to spin-glass-like behaviors, while the dynamic relaxation observed by  $\mu\text{SR}$  [4–8,97] exhibits nearly temperature-independent persistent quantum dynamics below the *cusp* temperature, associated with unusual hard-to-decouple line shapes. Similar behaviors were also observed in pyrochlore spin systems, such as  $\text{NaCaNi}_2\text{F}_7$  and  $\text{R}_2\text{Ti}_2\text{O}_7$  [98–100]. On the other hand, dynamic spin fluctuations die away at low temperatures well below  $T_g$  in typical dilute-alloy spin glasses CuMn, AuFe [78]. Figure 16 compares the dc susceptibility for  $\text{Fe}_{0.2}\text{Co}_{0.8}\text{Sn}$  and SCGO with similar  $T_g \sim 3.5$  K in ZFC mode under the external field of 1 kG. The inverse of susceptibility demonstrates a much larger frustration index  $|\theta_{\text{CW}}(150\text{--}300\text{ K})|/T_g = 340/3.5 \sim 97$  for SCGO as compared to 0.63 for  $\text{Fe}_{0.2}\text{Co}_{0.8}\text{Sn}$ . Note that  $|\theta_{\text{CW}}|$  is also very small in AuFe and CuMn [78]. The present study has identified that  $\text{Fe}_{0.2}\text{Co}_{0.8}\text{Sn}$  systems behave similarly to dilute-alloy spin glasses. The

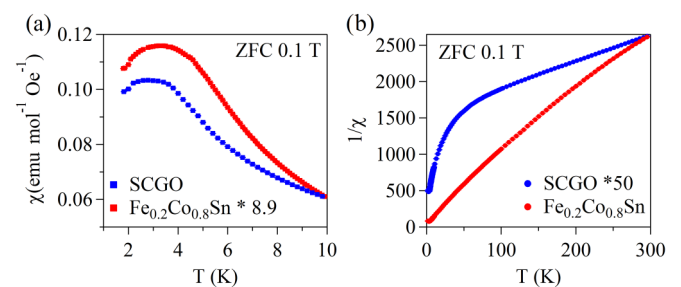


FIG. 16. Comparison of (a) dc susceptibility and (b) the inverse of dc susceptibility in ZFC mode under an external field of 1 kG. For better comparison, the dc susceptibility of  $\text{Fe}_{0.2}\text{Co}_{0.8}\text{Sn}$  was scaled by a factor of 8.9 in (a), while the inverse of the susceptibility of SCGO was scaled by a factor of 50.

internal field at the muon sites observed in  $\text{Fe}_{0.2}\text{Co}_{0.8}\text{Sn}$  is consistent in magnitude with the values expected for moments residing only on Fe atoms. In  $(\text{Fe}_{1-x}\text{Co}_x)\text{Sn}$  compounds, a spin-glass state appears when Fe concentration  $(1-x)$  becomes smaller than the percolation threshold 0.5 of kagome plane, and the spin freezing temperature  $T_g$  is proportional to the dilute Fe concentrations [45]. These features and similarities with CuMn and AuFe indicate that randomness and diluteness play primary roles in the origin of the spin glass behavior of  $(\text{Fe}, \text{Co})\text{Sn}$ . Although the kagome geometry leads to the flat band behaviors in band structures due to frustration in charge conduction in the underlying metallic lattice of CoSn, the present study demonstrates an example where dilute magnetic moments on the metallic kagome lattice exhibit classical spin glass behavior quite different from the spin-glass/spin-liquid behaviors often seen in insulating compounds with geometrical frustration of exchange interactions.

### ACKNOWLEDGMENTS

We greatly appreciate the support of the personnel at TRIUMF during the  $\mu\text{SR}$  measurements. The work at Columbia was supported by the U.S. NSF Grant No. DMR-2104661. S.T.M. measurements are supported by the Office of Basic Energy Sciences, Materials Sciences and Engineering Division, U.S. Department of Energy under Contract No. DE-SC0012704. The single crystal growth at Rice was supported

by U.S. DOE, BES under Grant No. DE-SC0012311 and by the Robert A. Welch Foundation under Grant No. C-1839 (P.D.). The work at Princeton University was supported by the Institute for Quantum Matter, an Energy Frontier Research Center funded by the U.S. Department of Energy (DOE), Office of Science, Basic Energy Sciences under Award No. DE-SC0019331. The work in TRIUMF/UBC/SBQMI was financially supported in part by the Max Planck–UBC–UTokyo Center for Quantum Materials and the Canada First Research Excellence Fund, the Quantum Materials and Future Technologies Program, and the Discovery Grant from the Natural Sciences and Engineering Research Council (NSERC) of Canada. Research at McMaster is supported by the NSERC of Canada. R.Q. and J.I. were supported by the U.S. NSF MRSEC program at Columbia through the Center for Precision-Assembled Quantum Materials (DMR-2011738). H.C.L. was supported by the National Key R&D Program of China (Grants No. 2022YFA1403800 and No. 2023YFA1406500) and National Natural Science Foundation of China (Grant No. 12274459). G.Q.Z. has received partial support from the Chinese Academy of Sciences Project for Young Scientists in Basic Research (2022YSBR-048).

### DATA AVAILABILITY

The data that support the findings of this article are openly available from the authors upon reasonable request.

- 
- [1] J. E. Greedan, Frustrated rare earth magnetism: Spin glasses, spin liquids and spin ices in pyrochlore oxides, *J. Alloys Compd.* **408–412**, 444 (2006).
- [2] J. S. Gardner, M. J. P. Gingras, and J. E. Greedan, Magnetic pyrochlore oxides, *Rev. Mod. Phys.* **82**, 53 (2010).
- [3] J. N. Reimers, J. E. Greedan, R. K. Kremer, E. Gmelin, and M. A. Subramanian, Short-range magnetic ordering in the highly frustrated pyrochlore  $\text{Y}_2\text{Mn}_2\text{O}_7$ , *Phys. Rev. B* **43**, 3387 (1991).
- [4] Y. J. Uemura, A. Keren, K. Kojima, L. P. Le, G. M. Luke, W. D. Wu, Y. Ajiro, T. Asano, Y. Kuriyama, M. Mekata, H. Kikuchi, and K. Kakurai, Spin fluctuations in frustrated kagomé lattice system  $\text{SrCr}_8\text{Ga}_4\text{O}_{19}$  studied by muon spin relaxation, *Phys. Rev. Lett.* **73**, 3306 (1994).
- [5] A. Keren, K. Kojima, L. P. Le, G. M. Luke, W. D. Wu, Y. J. Uemura, M. Takano, H. Dabkowska, and M. J. P. Gingras, Muon-spin-rotation measurements in the kagomé lattice systems: Cr-jarosite and Fe-jarosite, *Phys. Rev. B* **53**, 6451 (1996).
- [6] A. Keren, Y. J. Uemura, G. Luke, P. Mendels, M. Mekata, and T. Asano, Magnetic dilution in the geometrically frustrated  $\text{SrCr}_9\text{pGa}_{12-9p}\text{O}_{19}$  and the role of local dynamics: A muon spin relaxation study, *Phys. Rev. Lett.* **84**, 3450 (2000).
- [7] A. Fukaya, Y. Fudamoto, I. M. Gat, T. Ito, M. I. Larkin, A. T. Savici, Y. J. Uemura, P. P. Kyriakou, G. M. Luke, M. T. Rovers, K. M. Kojima, A. Keren, M. Hanawa, and Z. Hiroi, Muon spin relaxation and susceptibility studies of the pure and diluted spin  $\frac{1}{2}$  kagomé-like lattice system  $(\text{Cu}_x\text{Zn}_{1-x})_3\text{V}_2\text{O}_7(\text{OH})_2\cdot 2\text{H}_2\text{O}$ , *Phys. Rev. Lett.* **91**, 207603 (2003).
- [8] P. Mendels, F. Bert, M. A. de Vries, A. Olariu, A. Harrison, F. Duc, J. C. Trombe, J. S. Lord, A. Amato, and C. Baines, Quantum magnetism in the paratacamite family: Towards an ideal kagomé lattice, *Phys. Rev. Lett.* **98**, 077204 (2007).
- [9] J. S. Helton, K. Matan, M. P. Shores, E. A. Nytko, B. M. Bartlett, Y. Yoshida, Y. Takano, A. Suslov, Y. Qiu, J.-H. Chung, D. G. Nocera, and Y. S. Lee, Spin dynamics of the spin-1/2 kagome lattice antiferromagnet  $\text{ZnCu}_3(\text{OH})_6\text{Cl}_2$ , *Phys. Rev. Lett.* **98**, 107204 (2007).
- [10] Z. Hiroi, M. Hanawa, N. Kobayashi, M. Nohara, H. Takagi, Y. Kato, and M. Takigawa, Spin-1/2 Kagomé-like lattice in Volborthite  $\text{Cu}_3\text{V}_2\text{O}_7(\text{OH})_2\cdot 2\text{H}_2\text{O}$ , *J. Phys. Soc. Jpn.* **70**, 3377 (2001).
- [11] T.-H. Han, J. Singleton, and J. A. Schlueter, Barlowite: A spin-1/2 antiferromagnet with a geometrically perfect kagome motif, *Phys. Rev. Lett.* **113**, 227203 (2014).
- [12] Y. Wang, H. Wu, G. T. McCandless, J. Y. Chan, and M. N. Ali, Quantum states and intertwining phases in kagome materials, *Nat. Rev. Phys.* **5**, 635 (2023).
- [13] J.-X. Yin, B. Lian, and M. Z. Hasan, Topological kagome magnets and superconductors, *Nature (London)* **612**, 647 (2022).
- [14] E. Tang, J.-W. Mei, and X.-G. Wen, High-temperature fractional quantum Hall states, *Phys. Rev. Lett.* **106**, 236802 (2011).
- [15] K. Sun, Z. Gu, H. Katsura, and S. Das Sarma, Nearly flatbands with nontrivial topology, *Phys. Rev. Lett.* **106**, 236803 (2011).
- [16] D. Green, L. Santos, and C. Chamon, Isolated flat bands and spin-1 conical bands in two-dimensional lattices, *Phys. Rev. B* **82**, 075104 (2010).

- [17] S.-L. Yu and J.-X. Li, Chiral superconducting phase and chiral spin-density-wave phase in a Hubbard model on the kagome lattice, *Phys. Rev. B* **85**, 144402 (2012).
- [18] M. L. Kiesel, C. Platt, and R. Thomale, Unconventional Fermi surface instabilities in the kagome Hubbard model, *Phys. Rev. Lett.* **110**, 126405 (2013).
- [19] M. L. Kiesel and R. Thomale, Sublattice interference in the kagome Hubbard model, *Phys. Rev. B* **86**, 121105(R) (2012).
- [20] T. Li, M. Geier, J. Ingham, and H. D. Scammell, Higher-order topological superconductivity from repulsive interactions in kagome and honeycomb systems, *2D Mater.* **9**, 015031 (2022).
- [21] A. Wenger, A. Consiglio, H. Hohmann, M. Dürrnagel, F. O. von Rohr, H. D. Scammell, J. Ingham, D. Di Sante, and R. Thomale, Theory of unconventional magnetism in a Cu-based kagome metal, [arXiv:2411.03563](https://arxiv.org/abs/2411.03563).
- [22] H. D. Scammell, J. Ingham, T. Li, and O. P. Sushkov, Chiral excitonic order from twofold van Hove singularities in kagome metals, *Nat. Commun.* **14**, 605 (2023).
- [23] J. Ingham, A. Consiglio, D. di Sante, R. Thomale, and H. D. Scammell, Theory of excitonic order in  $\text{ScV}_6\text{Sn}_6$  and  $\text{LuNb}_6\text{Sn}_6$ , [arXiv:2410.16365](https://arxiv.org/abs/2410.16365).
- [24] J.-W. Dong, Z. Wang, and S. Zhou, Loop-current charge density wave driven by long-range Coulomb repulsion on the kagome lattice, *Phys. Rev. B* **107**, 045127 (2023).
- [25] J. B. Profe, L. Klebl, F. Grandi, H. Hohmann, M. Dürrnagel, T. Schwemmer, R. Thomale, and D. M. Kennes, Kagome Hubbard model from a functional renormalization group perspective, *Phys. Rev. Res.* **6**, 043078 (2024).
- [26] A. K. Nayak, J. E. Fischer, Y. Sun, B. Yan, J. Karel, A. C. Komarek, C. Shekhar, N. Kumar, W. Schnelle, J. Kübler, C. Felser, and S. S. P. Parkin, Large anomalous Hall effect driven by a nonvanishing Berry curvature in the noncolinear antiferromagnet  $\text{Mn}_3\text{Ge}$ , *Sci. Adv.* **2**, e1501870 (2016).
- [27] N. Kiyohara, T. Tomita, and S. Nakatsuji, Giant anomalous Hall effect in the chiral antiferromagnet  $\text{Mn}_3\text{Ge}$ , *Phys. Rev. Appl.* **5**, 064009 (2016).
- [28] S. Nakatsuji, N. Kiyohara, and T. Higo, Large anomalous Hall effect in a non-collinear antiferromagnet at room temperature, *Nature (London)* **527**, 212 (2015).
- [29] J. Kübler and C. Felser, Non-collinear antiferromagnets and the anomalous Hall effect, *Europhys. Lett.* **108**, 67001 (2014).
- [30] E. Liu, Y. Sun, N. Kumar, L. Muechler, A. Sun, L. Jiao, S.-Y. Yang, D. Liu, A. Liang, Q. Xu, J. Kroder, V. Süß, H. Borrmann, C. Shekhar, Z. Wang, C. Xi, W. Wang, W. Schnelle, S. Wirth, Y. Chen, S. T. B. Goennenwein, and C. Felser, Giant anomalous Hall effect in a ferromagnetic kagome-lattice semimetal, *Nat. Phys.* **14**, 1125 (2018).
- [31] D. F. Liu, A. J. Liang, E. K. Liu, Q. N. Xu, Y. W. Li, C. Chen, D. Pei, W. J. Shi, S. K. Mo, P. Dudin, T. Kim, C. Cacho, G. Li, Y. Sun, L. X. Yang, Z. K. Liu, S. S. P. Parkin, C. Felser, and Y. L. Chen, Magnetic Weyl semimetal phase in a kagome crystal, *Science* **365**, 1282 (2019).
- [32] S. N. Guin, P. Vir, Y. Zhang, N. Kumar, S. J. Watzman, C. Fu, E. Liu, K. Manna, W. Schnelle, J. Gooth, C. Shekhar, Y. Sun, and C. Felser, Zero-field Nernst effect in a ferromagnetic kagome-lattice Weyl-semimetal  $\text{Co}_3\text{Sn}_2\text{S}_2$ , *Adv. Mater.* **31**, 1806622 (2019).
- [33] P. K. Nag, R. Batabyal, J. Ingham, N. Morali, H. Tan, J. Koo, A. Consiglio, E. Liu, N. Avraham, R. Queiroz, R. Thomale, B. Yan, C. Felser, and H. Beidenkopf, Pomeranchuk instability induced by an emergent higher-order van Hove singularity on the distorted kagome surface of  $\text{Co}_3\text{Sn}_2\text{S}_2$ , [arXiv:2410.01994](https://arxiv.org/abs/2410.01994).
- [34] L. Ye, M. Kang, J. Liu, F. von Cube, C. R. Wicker, T. Suzuki, C. Jozwiak, A. Bostwick, E. Rotenberg, D. C. Bell, L. Fu, R. Comin, and J. G. Checkelsky, Massive Dirac fermions in a ferromagnetic kagome metal, *Nature (London)* **555**, 638 (2018).
- [35] L. Ye, M. K. Chan, R. D. McDonald, D. Graf, M. Kang, J. Liu, T. Suzuki, R. Comin, L. Fu, and J. G. Checkelsky, de Haas-van Alphen effect of correlated Dirac states in kagome metal  $\text{Fe}_3\text{Sn}_2$ , *Nat. Commun.* **10**, 4870 (2019).
- [36] S. Fang, L. Ye, M. P. Ghimire, M. Kang, J. Liu, M. Han, L. Fu, M. Richter, J. van den Brink, E. Kaxiras, R. Comin, and J. G. Checkelsky, Ferromagnetic helical nodal line and Kane-Mele spin-orbit coupling in kagome metal  $\text{Fe}_3\text{Sn}_2$ , *Phys. Rev. B* **105**, 035107 (2022).
- [37] Z. Hou, W. Ren, B. Ding, G. Xu, Y. Wang, B. Yang, Q. Zhang, Y. Zhang, E. Liu, F. Xu, W. Wang, G. Wu, X. Zhang, B. Shen, and Z. Zhang, Observation of various and spontaneous magnetic skyrmionic bubbles at room temperature in a frustrated kagome magnet with uniaxial magnetic anisotropy, *Adv. Mater.* **29**, 1701144 (2017).
- [38] Q. Du, M.-G. Han, Y. Liu, W. Ren, Y. Zhu, and C. Petrovic, Room-temperature skyrmion thermopower in  $\text{Fe}_3\text{Sn}_2$ , *Adv. Quantum Technol.* **3**, 2000058 (2020).
- [39] L. Kong, J. Tang, W. Wang, Y. Wu, J. Jiang, Y. Wang, J. Li, Y. Xiong, M. Tian, and H. Du, Observation of hybrid magnetic skyrmion bubbles in  $\text{Fe}_3\text{Sn}_2$  nanodisks, *Phys. Rev. B* **107**, 174425 (2023).
- [40] J.-X. Yin, S. S. Zhang, H. Li, K. Jiang, G. Chang, B. Zhang, B. Lian, C. Xiang, I. Belopolski, H. Zheng, T. A. Cochran, S.-Y. Xu, G. Bian, K. Liu, T.-R. Chang, H. Lin, Z.-Y. Lu, Z. Wang, S. Jia, W. Wang, and M. Z. Hasan, Giant and anisotropic many-body spin-orbit tunability in a strongly correlated kagome magnet, *Nature (London)* **562**, 91 (2018).
- [41] M. Kang, L. Ye, S. Fang, J.-S. You, A. Levitan, M. Han, J. I. Facio, C. Jozwiak, A. Bostwick, E. Rotenberg, M. K. Chan, R. D. McDonald, D. Graf, K. Kaznatcheev, E. Vescovo, D. C. Bell, E. Kaxiras, J. van den Brink, M. Richter, M. Prasad Ghimire, J. G. Checkelsky, and R. Comin, Dirac fermions and flat bands in the ideal kagome metal  $\text{FeSn}$ , *Nat. Mater.* **19**, 163 (2020).
- [42] M. Kang, S. Fang, L. Ye, H. C. Po, J. Denlinger, C. Jozwiak, A. Bostwick, E. Rotenberg, E. Kaxiras, J. G. Checkelsky, and R. Comin, Topological flat bands in frustrated kagome lattice  $\text{CoSn}$ , *Nat. Commun.* **11**, 4004 (2020).
- [43] Y. Xie, L. Chen, T. Chen, Q. Wang, Q. Yin, J. R. Stewart, M. B. Stone, L. L. Daemen, E. Feng, H. Cao, H. Lei, Z. Yin, A. H. MacDonald, and P. Dai, Spin excitations in metallic kagome lattice  $\text{FeSn}$  and  $\text{CoSn}$ , *Commun. Phys.* **4**, 240 (2021).
- [44] B. C. Sales, J. Yan, W. R. Meier, A. D. Christianson, S. Okamoto, and M. A. McGuire, Electronic, magnetic, and thermodynamic properties of the kagome layer compound  $\text{FeSn}$ , *Phys. Rev. Mater.* **3**, 114203 (2019).
- [45] B. C. Sales, W. R. Meier, A. F. May, J. Xing, J.-Q. Yan, S. Gao, Y. H. Liu, M. B. Stone, A. D. Christianson, Q. Zhang, and M. A. McGuire, Tuning the flat bands of the kagome metal  $\text{CoSn}$  with Fe, In, or Ni doping, *Phys. Rev. Mater.* **5**, 044202 (2021).

- [46] M. Han, H. Inoue, S. Fang, C. John, L. Ye, M. K. Chan, D. Graf, T. Suzuki, M. P. Ghimire, W. J. Cho, E. Kaxiras, and J. G. Checkelsky, Evidence of two-dimensional flat band at the surface of antiferromagnetic kagome metal FeSn, *Nat. Commun.* **12**, 5345 (2021).
- [47] Z. Lin, C. Wang, P. Wang, S. Yi, L. Li, Q. Zhang, Y. Wang, Z. Wang, H. Huang, Y. Sun, Y. Huang, D. Shen, D. Feng, Z. Sun, J.-H. Cho, C. Zeng, and Z. Zhang, Dirac fermions in antiferromagnetic FeSn kagome lattices with combined space inversion and time-reversal symmetry, *Phys. Rev. B* **102**, 155103 (2020).
- [48] H. Zhang, B. D. Oli, Q. Zou, X. Guo, Z. Wang, and L. Li, Visualizing symmetry-breaking electronic orders in epitaxial kagome magnet FeSn films, *Nat. Commun.* **14**, 6167 (2023).
- [49] H. W. Suriya Arachchige, W. R. Meier, M. Marshall, T. Matsuoka, R. Xue, M. A. McGuire, R. P. Hermann, H. Cao, and D. Mandrus, Charge density wave in kagome lattice intermetallic ScV<sub>6</sub>Sn<sub>6</sub>, *Phys. Rev. Lett.* **129**, 216402 (2022).
- [50] D. Di Sante, C. Bigi, P. Eck, S. Enzner, A. Consiglio, G. Pokharel, P. Carrara, P. Orgiani, V. Polewczyk, J. Fujii, P. D. C. King, I. Vobornik, G. Rossi, I. Zeljkovic, S. D. Wilson, R. Thomale, G. Sangiovanni, G. Panaccione, and F. Mazzola, Flat band separation and robust spin Berry curvature in bilayer kagome metals, *Nat. Phys.* **19**, 1135 (2023).
- [51] A. Korshunov, H. Hu, D. Subires, Y. Jiang, D. Călugăru, X. Feng, A. Rajapitamahuni, C. Yi, S. Roychowdhury, M. G. Vergniory, J. Stempfer, C. Shekhar, E. Vescovo, D. Chernyshov, A. H. Said, A. Bosak, C. Felser, B. A. Bernevig, and S. Blanco-Canosa, Softening of a flat phonon mode in the kagome ScV<sub>6</sub>Sn<sub>6</sub>, *Nat. Commun.* **14**, 6646 (2023).
- [52] G. Pokharel, B. R. Ortiz, L. Kautzsch, S. J. Gomez Alvarado, K. Mallayya, G. Wu, E.-A. Kim, J. P. C. Ruff, S. Sarker, and S. D. Wilson, Frustrated charge order and cooperative distortions in ScV<sub>6</sub>Sn<sub>6</sub>, *Phys. Rev. Mater.* **7**, 104201 (2023).
- [53] S. Cao, C. Xu, H. Fukui, T. Manjo, Y. Dong, M. Shi, Y. Liu, C. Cao, and Y. Song, Competing charge-density wave instabilities in the kagome metal ScV<sub>6</sub>Sn<sub>6</sub>, *Nat. Commun.* **14**, 7671 (2023).
- [54] A. K. Kundu, X. Huang, E. Seewald, E. Ritz, S. Pakhira, S. Zhang, D. Sun, S. Turkel, S. Shabani, T. Yilmaz, E. Vescovo, C. R. Dean, D. C. Johnston, T. Valla, T. Birol, D. N. Basov, R. M. Fernandes, and A. N. Pasupathy, Low-energy electronic structure in the unconventional charge-ordered state of ScV<sub>6</sub>Sn<sub>6</sub>, *Nat. Commun.* **15**, 5008 (2024).
- [55] S. Lee, C. Won, J. Kim, J. Yoo, S. Park, J. Denlinger, C. Jozwiak, A. Bostwick, E. Rotenberg, R. Comin, M. Kang, and J.-H. Park, Nature of charge density wave in kagome metal ScV<sub>6</sub>Sn<sub>6</sub>, *npj Quantum Mater.* **9**, 15 (2024).
- [56] Y.-X. Jiang, S. Shao, W. Xia, M. M. Denner, J. Ingham, M. S. Hossain, Q. Qiu, X. Zheng, H. Chen, Z.-J. Cheng, X. P. Yang, B. Kim, J.-X. Yin, S. Zhang, M. Litskevich, Q. Zhang, T. A. Cochran, Y. Peng, G. Chang, Y. Guo, R. Thomale, T. Neupert, and M. Z. Hasan, Van Hove annihilation and nematic instability on a kagome lattice, *Nat. Mater.* **23**, 1214 (2024).
- [57] B. R. Ortiz, W. R. Meier, G. Pokharel, J. Chamorro, F. Yang, S. Mozaffari, A. Thaler, S. J. Gomez Alvarado, H. Zhang, D. S. Parker, G. D. Samolyuk, J. A. M. Paddison, J. Yan, F. Ye, S. Sarker, S. D. Wilson, H. Miao, D. Mandrus, and M. A. McGuire, Stability frontiers in the AM<sub>6</sub>X<sub>6</sub> kagome metals: The LnNb<sub>6</sub>Sn<sub>6</sub> (Ln:Ce-Lu,Y) family and density-wave transition in LuNb<sub>6</sub>Sn<sub>6</sub>, *J. Am. Chem. Soc.* **147**, 5279 (2025).
- [58] B. R. Ortiz, S. M. L. Teicher, Y. Hu, J. L. Zuo, P. M. Sarte, E. C. Schueller, A. M. Milinda Abeykoon, M. J. Krogstad, S. Rosenkranz, R. Osborn, R. Seshadri, L. Balents, J. He, and S. D. Wilson, CsV<sub>3</sub>Sb<sub>5</sub>: A Z<sub>2</sub> topological kagome metal with a superconducting ground state, *Phys. Rev. Lett.* **125**, 247002 (2020).
- [59] B. R. Ortiz, S. M. L. Teicher, L. Kautzsch, P. M. Sarte, N. Ratcliff, J. Harter, J. P. C. Ruff, R. Seshadri, and S. D. Wilson, Fermi surface mapping and the nature of charge-density-wave order in the kagome superconductor CsV<sub>3</sub>Sb<sub>5</sub>, *Phys. Rev. X* **11**, 041030 (2021).
- [60] Y. Xu, Z. Ni, Y. Liu, B. R. Ortiz, Q. Deng, S. D. Wilson, B. Yan, L. Balents, and L. Wu, Three-state nematicity and magneto-optical Kerr effect in the charge density waves in kagome superconductors, *Nat. Phys.* **18**, 1470 (2022).
- [61] Y.-X. Jiang, J.-X. Yin, M. M. Denner, N. Shumiya, B. R. Ortiz, G. Xu, Z. Guguchia, J. He, M. S. Hossain, X. Liu, J. Ruff, L. Kautzsch, S. S. Zhang, G. Chang, I. Belopolski, Q. Zhang, T. A. Cochran, D. Multer, M. Litskevich, Z.-J. Cheng, X. P. Yang, Z. Wang, R. Thomale, T. Neupert, S. D. Wilson, and M. Z. Hasan, Unconventional chiral charge order in kagome superconductor KV<sub>3</sub>Sb<sub>5</sub>, *Nat. Mater.* **20**, 1353 (2021).
- [62] C. Mielke III, D. Das, J.-X. Yin, H. Liu, R. Gupta, Y.-X. Jiang, M. Medarde, X. Wu, H. C. Lei, J. Chang, P. Dai, Q. Si, H. Miao, R. Thomale, T. Neupert, Y. Shi, R. Khasanov, M. Z. Hasan, H. Luetkens, and Z. Guguchia, Time-reversal symmetry-breaking charge order in a kagome superconductor, *Nature (London)* **602**, 245 (2022).
- [63] H. Chen, H. Yang, B. Hu, Z. Zhao, J. Yuan, Y. Xing, G. Qian, Z. Huang, G. Li, Y. Ye, S. Ma, S. Ni, H. Zhang, Q. Yin, C. Gong, Z. Tu, H. Lei, H. Tan, S. Zhou, C. Shen, X. Dong, B. Yan, Z. Wang, and H.-J. Gao, Roton pair density wave in a strong-coupling kagome superconductor, *Nature (London)* **599**, 222 (2021).
- [64] Z. Liang, X. Hou, F. Zhang, W. Ma, P. Wu, Z. Zhang, F. Yu, J.-J. Ying, K. Jiang, L. Shan, Z. Wang, and X.-H. Chen, Three-dimensional charge density wave and surface-dependent vortex-core states in a kagome superconductor CsV<sub>3</sub>Sb<sub>5</sub>, *Phys. Rev. X* **11**, 031026 (2021).
- [65] H. Li, H. Zhao, B. R. Ortiz, T. Park, M. Ye, L. Balents, Z. Wang, S. D. Wilson, and I. Zeljkovic, Rotation symmetry breaking in the normal state of a kagome superconductor KV<sub>3</sub>Sb<sub>5</sub>, *Nat. Phys.* **18**, 265 (2022).
- [66] L. Nie, K. Sun, W. Ma, D. Song, L. Zheng, Z. Liang, P. Wu, F. Yu, J. Li, M. Shan, D. Zhao, S. Li, B. Kang, Z. Wu, Y. Zhou, K. Liu, Z. Xiang, J. Ying, Z. Wang, T. Wu, and X. Chen, Charge-density-wave-driven electronic nematicity in a kagome superconductor, *Nature (London)* **604**, 59 (2022).
- [67] Z. Liu, Y. Shi, Q. Jiang, E. W. Rosenberg, J. M. DeStefano, J. Liu, C. Hu, Y. Zhao, Z. Wang, Y. Yao, D. Graf, P. Dai, J. Yang, X. Xu, and J.-H. Chu, Absence of E<sub>2g</sub> nematic instability and dominant A<sub>1g</sub> response in the kagome metal CsV<sub>3</sub>Sb<sub>5</sub>, *Phys. Rev. X* **14**, 031015 (2024).
- [68] C. Guo, C. Putzke, S. Konyzheva, X. Huang, M. Gutierrez-Amigo, I. Errea, D. Chen, M. G. Vergniory, C. Felser, M. H. Fischer, T. Neupert, and P. J. W. Moll, Switchable chiral transport in charge-ordered kagome metal CsV<sub>3</sub>Sb<sub>5</sub>, *Nature (London)* **611**, 461 (2022).
- [69] T. Asaba, A. Onishi, Y. Kageyama, T. Kiyosue, K. Ohtsuka, S. Suetsugu, Y. Kohsaka, T. Gaggli, Y. Kasahara, H. Murayama,

- K. Hashimoto, R. Tazai, H. Kontani, B. R. Ortiz, S. D. Wilson, Q. Li, H.-H. Wen, T. Shibauchi, and Y. Matsuda, Evidence for an odd-parity nematic phase above the charge-density-wave transition in a kagome metal, *Nat. Phys.* **20**, 40 (2024).
- [70] C. Guo, G. Wagner, C. Putzke, D. Chen, K. Wang, L. Zhang, M. Gutierrez-Amigo, I. Errea, M. G. Vergniory, C. Felser, M. H. Fischer, T. Neupert, and P. J. W. Moll, Correlated order at the tipping point in the kagome metal  $\text{CsV}_3\text{Sb}_5$ , *Nat. Phys.* **20**, 579 (2024).
- [71] M. S. Hossain, Q. Zhang, J. Ingham, J. Liu, S. Shao, Y. Li, Y. Wang, B. K. Pokharel, Z.-J. Cheng, Y.-X. Jiang, M. Litskevich, B. Kim, X. Yang, Y. Li, T. A. Cochran, Y. Yao, D. Popović, Z. Wang, G. Chang, R. Thomale, L. Balicas, and M. Z. Hasan, Field induced density wave in a kagome superconductor, [arXiv:2501.13260](https://arxiv.org/abs/2501.13260).
- [72] S. D. Wilson and B. R. Ortiz,  $\text{AV}_3\text{Sb}_5$  kagome superconductors, *Nat. Rev. Mater.* **9**, 420 (2024).
- [73] K. Jiang, T. Wu, J.-X. Yin, Z. Wang, M. Z. Hasan, S. D. Wilson, X. Chen, and J. Hu, Kagome superconductors  $\text{AV}_3\text{Sb}_5$  ( $A = \text{K}, \text{Rb}, \text{Cs}$ ), *Natl. Sci. Rev.* **10**, nwac199 (2023).
- [74] X. Teng, L. Chen, F. Ye, E. Rosenberg, Z. Liu, J.-X. Yin, Y.-X. Jiang, J. S. Oh, M. Z. Hasan, K. J. Neubauer, B. Gao, Y. Xie, M. Hashimoto, D. Lu, C. Jozwiak, A. Bostwick, E. Rotenberg, R. J. Birgeneau, J.-H. Chu, M. Yi, and P. Dai, Discovery of charge density wave in a kagome lattice antiferromagnet, *Nature (London)* **609**, 490 (2022).
- [75] S. J. Blundell, R. De Renzi, T. Lancaster, and F. L. Pratt, *Muon Spectroscopy: An Introduction* (Oxford University Press, Oxford, 2021).
- [76] O. Hartmann and R. Wäppling, Muon spin precession in the hexagonal antiferromagnet FeSn, *Phys. Scr.* **35**, 499 (1987).
- [77] W. R. Meier, J. Yan, M. A. McGuire, X. Wang, A. D. Christianson, and B. C. Sales, Reorientation of antiferromagnetism in cobalt doped FeSn, *Phys. Rev. B* **100**, 184421 (2019).
- [78] Y. J. Uemura, T. Yamazaki, D. R. Harshman, M. Senba, and E. J. Ansaldo, Muon-spin relaxation in  $\text{AuFe}$  and  $\text{CuMn}$  spin glasses, *Phys. Rev. B* **31**, 546 (1985).
- [79] A. Suter and B. M. Wojek, Musrfit: A free platform-independent framework for  $\mu\text{SR}$  data analysis, *Phys. Procedia* **30**, 69 (2012).
- [80] W. R. Meier, M.-H. Du, S. Okamoto, N. Mohanta, A. F. May, M. A. McGuire, C. A. Bridges, G. D. Samolyuk, and B. C. Sales, Flat bands in the  $\text{CoSn}$ -type compounds, *Phys. Rev. B* **102**, 075148 (2020).
- [81] Z. Liu, M. Li, Q. Wang, G. Wang, C. Wen, K. Jiang, X. Lu, S. Yan, Y. Huang, D. Shen, J.-X. Yin, Z. Wang, Z. Yin, H. Lei, and S. Wang, Orbital-selective Dirac fermions and extremely flat bands in frustrated kagome-lattice metal  $\text{CoSn}$ , *Nat. Commun.* **11**, 4002 (2020).
- [82] M. Kakihana, K. Nishimura, D. Aoki, A. Nakamura, M. Nakashima, Y. Amako, T. Takeuchi, T. Kida, T. Tahara, M. Hagiwara, H. Harima, M. Hedo, T. Nakama, and Y. Ōnuki, Electronic states of antiferromagnet FeSn and Pauli paramagnet  $\text{CoSn}$ , *J. Phys. Soc. Jpn.* **88**, 014705 (2019).
- [83] H. Li, H. Zhao, Q. Yin, Q. Wang, Z. Ren, S. Sharma, H. Lei, Z. Wang, and I. Zeljkovic, Spin-polarized imaging of the antiferromagnetic structure and field-tunable bound states in kagome magnet FeSn, *Sci. Rep.* **12**, 14525 (2022).
- [84] D. Multer, J.-X. Yin, M. S. Hossain, X. Yang, B. C. Sales, H. Miao, W. R. Meier, Y.-X. Jiang, Y. Xie, P. Dai, J. Liu, H. Deng, H. Lei, B. Lian, and M. Zahid Hasan, Imaging real-space flat band localization in kagome magnet FeSn, *Commun. Mater.* **4**, 17 (2023).
- [85] N. Nishida, R. Hayano, K. Nagamine, T. Yamazaki, J. Brewer, D. Garner, D. Fleming, T. Takeuchi, and Y. Ishikawa, Hyperfine field and diffusion of  $\mu^+$  in Fe single crystals, *Solid State Commun.* **22**, 235 (1977).
- [86] I. J. Onuorah, P. Bonfà, and R. De Renzi, Muon contact hyperfine field in metals: A DFT calculation, *Phys. Rev. B* **97**, 174414 (2018).
- [87] D. Tse and S. R. Hartmann, Nuclear spin-lattice relaxation via paramagnetic centers without spin diffusion, *Phys. Rev. Lett.* **21**, 511 (1968).
- [88] H. Miao, T. T. Zhang, H. X. Li, G. Fabbris, A. H. Said, R. Tartaglia, T. Yilmaz, E. Vescovo, J.-X. Yin, S. Murakami, X. L. Feng, K. Jiang, X. L. Wu, A. F. Wang, S. Okamoto, Y. L. Wang, and H. N. Lee, Signature of spin-phonon coupling driven charge density wave in a kagome magnet, *Nat. Commun.* **14**, 6183 (2023).
- [89] S. A. López-Paz, Z. Guguchia, V. Y. Pomjakushin, C. Witteveen, A. Cervellino, H. Luetkens, N. Casati, A. F. Morpurgo, and F. O. von Rohr, Dynamic magnetic crossover at the origin of the hidden-order in van der Waals antiferromagnet  $\text{CrSBr}$ , *Nat. Commun.* **13**, 4745 (2022).
- [90] C. Mielke III, W. L. Ma, V. Pomjakushin, O. Zaharko, S. Sturniolo, X. Liu, V. Ukleev, J. S. White, J.-X. Yin, S. S. Tsirkin, C. B. Larsen, T. A. Cochran, M. Medarde, V. Porée, D. Das, R. Gupta, C. N. Wang, J. Chang, Z. Q. Wang, R. Khasanov, T. Neupert, A. Amato, L. Liborio, S. Jia, M. Z. Hasan, H. Luetkens, and Z. Guguchia, Low-temperature magnetic crossover in the topological kagome magnet  $\text{TbMn}_6\text{Sn}_6$ , *Commun. Phys.* **5**, 107 (2022).
- [91] L. Häggström, T. Ericsson, R. Wäppling, and K. Chandra, Studies of the magnetic structure of FeSn using the Mössbauer effect, *Phys. Scr.* **11**, 47 (1975).
- [92] S. K. Kulshreshtha and P. Raj, Anisotropic hyperfine fields in FeSn by Mössbauer spectroscopy, *J. Phys. F* **11**, 281 (1981).
- [93] S. Ligenza, A spin-flip effect in FeSn, *Phys. Status Solidi (b)* **45**, 721 (1971).
- [94] X. Obradors, A. Labarta, A. Isalgué, J. Tejada, J. Rodriguez, and M. Pernet, Magnetic frustration and lattice dimensionality in  $\text{SrCr}_8\text{Ga}_4\text{O}_{19}$ , *Solid State Commun.* **65**, 189 (1988).
- [95] M. G. Townsend, G. Longworth, and E. Roudaut, Triangular-spin, kagome plane in jarosites, *Phys. Rev. B* **33**, 4919 (1986).
- [96] M. Lafontaine, A. Le Bail, and G. Férey, Copper-containing minerals—I.  $\text{Cu}_3\text{V}_2\text{O}_7(\text{OH})_2 \cdot 2\text{H}_2\text{O}$ : The synthetic homolog of volborthite; crystal structure determination from x-ray and neutron data; structural correlations, *J. Solid State Chem.* **85**, 220 (1990).
- [97] F. Bert, D. Bono, P. Mendels, J.-C. Trombe, P. Millet, A. Amato, C. Baines, and A. Hillier, Dilution in volborthite  $S = 1/2$  frustrated magnet: a  $\mu\text{SR}$  and NMR study, *J. Phys.: Condens. Matter* **16**, S829 (2004).
- [98] Y. Cai, M. N. Wilson, A. M. Hallas, L. Liu, B. A. Frandsen, S. R. Dunsiger, J. W. Krizan, R. J. Cava, O. Rubel, Y. J. Uemura, and G. M. Luke,  $\mu\text{SR}$  study of spin freezing and persistent spin dynamics in  $\text{NaCaNi}_2\text{F}_7$ , *J. Phys.: Condens. Matter* **30**, 385802 (2018).

- [99] J. Lago, T. Lancaster, S. J. Blundell, S. T. Bramwell, F. L. Pratt, M. Shirai, and C. Baines, Magnetic ordering and dynamics in the XY pyrochlore antiferromagnet: A muon-spin relaxation study of  $\text{Er}_2\text{Ti}_2\text{O}_7$  and  $\text{Er}_2\text{Sn}_2\text{O}_7$ , *J. Phys.: Condens. Matter* **17**, 979 (2005).
- [100] P. Dalmas de Réotier, A. Maisuradze, and A. Yaouanc, Recent  $\mu\text{SR}$  studies of insulating rare-earth pyrochlore magnets, *J. Phys. Soc. Jpn.* **85**, 091010 (2016).